DETERMINING STAND AGES IN A HYPERSPECTRAL IMAGE USING ARTIFICIAL NEURAL NETWORKS

by

ZACHARY JARED BORTOLOT

Sc. B., Brown University, 1997

A THESIS SUBMITTED IN PARTIAL FULFILLMENT OF
THE REQUIREMENTS FOR THE DEGREE OF

MASTER OF SCIENCE

in

THE FACULTY OF FORESTRY

DEPARTMENT OF FOREST RESOURCES MANAGEMENT

We accept this thesis as conforming
to the required standard

THE UNIVERSITY OF BRITISH COLUMBIA

July 2000

Department of Forest Resources Management

The University of British Columbia
Vancouver, Canada

Date August 25, 2000

ABSTRACT

An Airborne Visible / Infrared Imaging Spectrometer (AVIRIS) image was analysed to assess the feasibility of using feed-forward artificial neural networks to determine stand ages in the Sooke watershed located in southern Vancouver Island. Training data were systematically collected at the pixel level from photo interpreted forest cover data of the site. Artificial neural networks having a variety of architectures were trained using these data in conjunction with several different learning parameters. Once the neural networks were trained, all pixels in the area of interest were analysed and assigned an age. These pixel-level ages were used to extrapolate the ages of the forest cover polygons, and the ages were compared to the photointerpreted polygon ages. Results showed that a good correspondence existed, especially for larger polygons. However, accurate results could be obtained using a subset of the bands and data simulating Landsat TM bands 2 through 5 and 7. The use of topographic and view angle data in addition to the spectral data produced equivalent or slightly poorer results than the spectral data on its own. The use of a first difference image did not improve the prediction accuracy. The results of this study suggest that the technique used may be a reasonable means of determining the ages of forest stands, and may be a good choice when ground data on stand ages are available but collecting and interpreting aerial photographs is prohibitively expensive. This will especially be the case when data from satellite-mounted hyperspectral sensors become available in late 2000.

TABLE OF CONTENTS

Abstract....ii

List of Tables....iv

List of Figures....v

Acknowledgements....vi

CHAPTER I Introduction....1

1.1 Spectral response of vegetation....2
1.2 Changes in canopy reflectrance with stand age....4
1.3 Previous research....5
1.4 Artificial neural networks....7
1.5 Objective of study....9
1.6 Study site and available data....10

CHAPTER II Method....14

2.1 Image preparation....14
2.2 Georeferencing the AVIRIS data....15
2.3 Rasterizing the forest cover data....18
2.4 Creating topographic and view angle data....18
2.5 Eliminating noisy bands....18
2.6 Creating first difference images....18
2.7 Creating the training data....19
2.8 Processing the data....20

CHAPTER III Results and discussion....24

CHAPTER IV Conclusions....32

Bibliography....34

Appendix I Wavelengths of the AVIRIS channels used in the study....39

Appendix II Results for polygons containing pure Douglas-fir stands....45

Appendix III Results for all polygons regardless of species present....48

Appendix IV Glossary of terms....51

LIST OF TABLES

Table 1a: Attributes of pure Douglas-fir stands.....13

Table 1b: Attributes of all stands.....13

Table 2: Neural network architectures and training parameters used in this study.....21

Table 3a, 3b: The best results for each training set.....25

Tables 4a, 4b, 4c: Confusion matrices for the pure Douglas-fir stands.....26

Tables 5a, 5b, 5c: Confusion matrices for all stands in the study area.....27

LIST OF FIGURES

Figure 1: The canopy-level reflectance of four age classes of Douglas-fir....3

Figure 2: A typical artificial neural network....8

Figure 3: Location of the study site....11

Figure 4: The AVIRIS scene....12

Figure 5: Pitch, roll and altitude during image acquisition....17

Figure 6a: Photo-interpreted stand ages for pure Douglas-fir stands in the study area....28

Figure 6b: Ages determined for pure Douglas-fir stands using an artificial neural network....29

Figure 7a: Photo-interpreted stand ages for all stands in the study area....30

Figure 7b: Ages determined for all stands using an artificial neural network....31

ACKNOWLEDGEMENTS

I would like to acknowledge several people and organisations who contributed greatly to this research project and to my graduate education. First I would like to acknowledge my advisor, Dr. Peter Murtha, whose incredible passion for remote sensing made me realise that remote sensing is an art and that remote sensed images are not just grids of numbers. Additionally his open minded approach to advising allowed me to find my own niche in remote sensing rather than being pushed along a set path.

Next I would like to thank the members of my committee, Drs. Peter Marshall and David Lowe, for their thoughtful reviews of this paper and for their useful advice on statistics and neural networks respectively.

I am also very grateful to the Pacific Forestry Centre division of Natural Resources Canada for providing the AVIRIS data used in this analysis, and to the Capitol Regional District for providing the forest cover, road and elevation data.

Finally I would like to thank the Van Dusen Foundation for helping to fund my degree.

CHAPTER I: Introduction

Knowledge of the ages of forest stands is important in many aspects of forest management. These aspects include ensuring a sustainable wood supply, preserving biodiversity (BC Ministry of Forests, 1995b), and predicting susceptibility to forest pests such as mountain pine beetle (BC Ministry of Forests, 1995a), defoliating insects (BC Ministry of Forests, 1995c) and pine stem rusts (BC Ministry of Forests, 1996).

In British Columbia, the ages of stands have been estimated for most forested Crown land. Estimated ages were mapped between 1963 and 1973 at a scale of either 1:15,840 or 1:31,680, generally based on interpretation of medium scale panchromatic air photos[1] (BC Ministry of Forests, 1998a). After the maps were completed, the boundaries of areas affected by harvesting or natural forest depletions were incorporated into the map using visually interpreted Landsat TM or SPOT satellite imagery or ground GPS surveys, and the stand ages were projected forward from the initial estimates[1] (BC Ministry of Forests, 1998a).

Unfortunately, determining stand age from medium scale aerial photographs is quite difficult, and relies on the photo interpreter using many subtle clues relating to stand structure, species composition and site history[1]. Although the BC Ministry of Forests' published guidelines for the Vegetation Resources Inventory currently being undertaken specify that the interpreted ages of the primary and secondary species within a stand be accurate to within 5 years for trees less than 41 years old, 20 years for trees between 41 and 250 years old and 100 years for trees over 251 years old (BC Ministry of Forests, 1998b), many managers find that the ages on existing forest cover maps are quite unreliable[2]. Additionally, changes may have taken place in the forests since the forest cover maps were originally produced which were not subsequently incorporated into the maps.

This paper will examine the potential of a digital remote sensing approach for mapping stand ages. There are several advantages a digital approach has over a visual one:

1. It is less time consuming (Billingsley, 1983)
2. It is less subjective (Billingsley, 1983)
3. According to the Young-Helmholtz theory, (Avery and Berlin, 1992; p. 33) human interpreters can only view a maximum of three bands simultaneously, since all perceived colours consist of combinations of red, green and blue light. Many digital

---

[1]X. Yuan, Resources Inventory Branch, BC Ministry of Forests, *pers. comm.*, October 28, 1999

[2]J. Thurston, Registered Professional Forester, Plateau Forest Products, *pers. comm.*, August 12, 1999

techniques, such as maximum likelihood classification, can handle a much greater number (Avery and Berlin, 1992; p. 451-452). The spectral features discussed in subsequent sections would be difficult to use in conjunction with one another if only three bands could be used at a time.

Additionally, digital imagery is often much less expensive to acquire than aerial photography, especially if the digital sensor being used is mounted on a satellite. Combined with the decreased amount of processing time, this would make frequent forest cover updates more economical.

1.1 Spectral response of vegetation

Most conventional remote sensing techniques rely on the interaction of light with the material of interest. Each wavelength of light interacts differently with different surface materials, and differences exist among individual cover types. These differences allow scene components to be distinguished from one another. At the wavelengths of light examined in this study (0.4 to 2.5 μm), the interaction is most commonly expressed in terms of reflectance. Reflectance is the ratio of the flux of light energy at a given wavelength which is not absorbed or transmitted by a body to the flux of light at the same wavelength which is incident upon it (National Aeronautics and Space Administration, 2000). Figure 1 shows the reflectance at different wavelengths for stands of Douglas-fir (*Pseudotsuga menziesii* (Mirb.) Franco).

There are a number of features which are apparent in these curves:

1. Wavelengths below 0.7μm: the visible light region

The shape of the spectral reflectance curve in this region is dominated by pigments. Pigments are complex organic molecules found in the plant leaves which absorb light at specific wavelengths. They absorb light by means of electronic transitions: in the pigment there is a group of atoms known as the chromophore which are surrounded by a shell of delocalised electrons known as a π shell. When light at the right wavelength strikes this shell, the shell is reconfigured to a higher energy state, causing an absorption (Lawlor, 1987; pp. 22-25).

Although several pigments contribute to the spectral curve, the most significant contributions come from chlorophyll-a and chlorophyll-b, which cause broad absorptions centered at 0.445 and 0.645 μm (Gates *et al.*, 1965). The grana found in the leaves' chloroplasts are approximately 0.5 μm long. This causes light with wavelengths of about 0.5 μm to be scattered, increasing the leaves' reflectance at these wavelengths (Gates *et al.*, 1965).

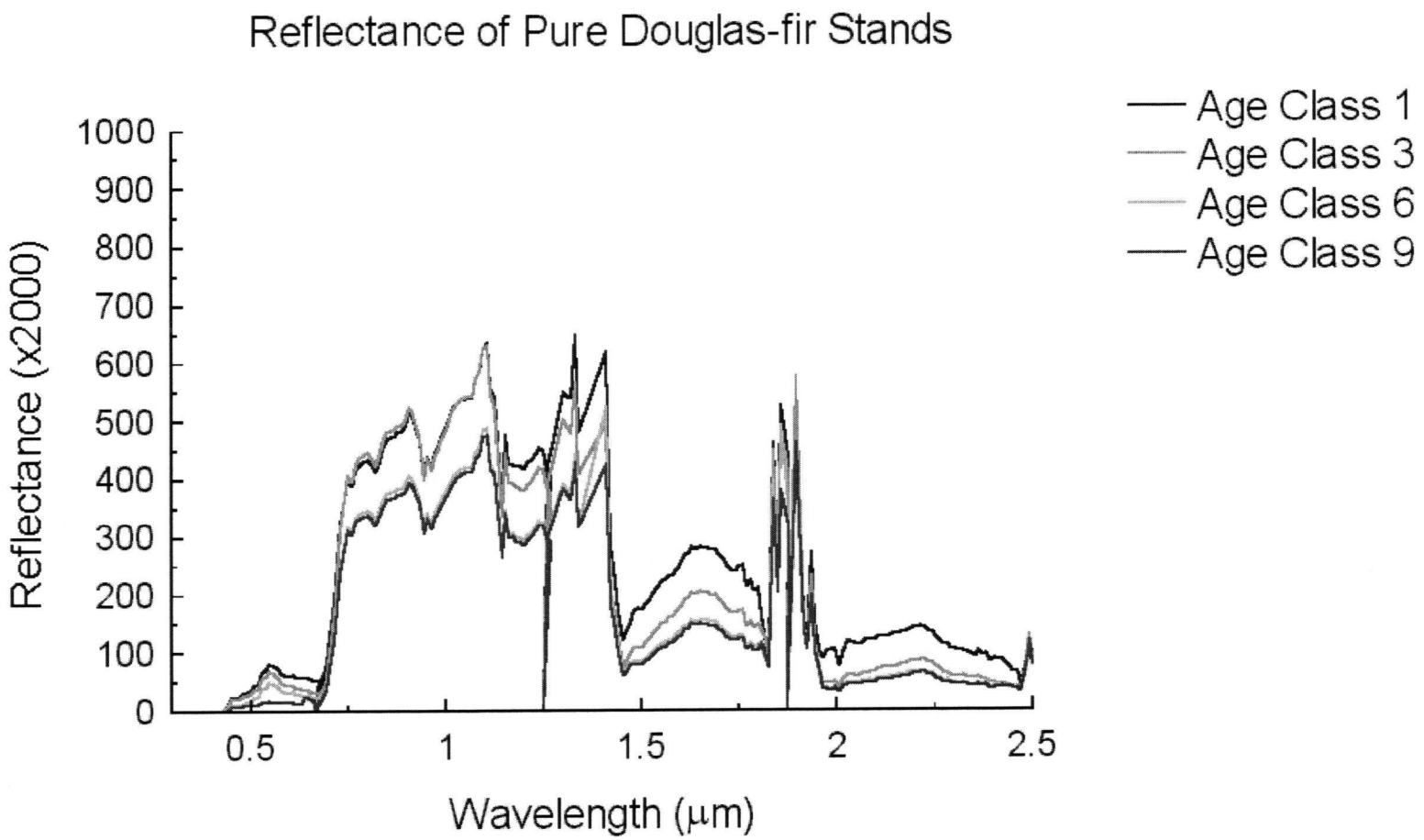

Figure 1: The canopy-level reflectance of four age classes of Douglas-fir
The data were acquired from the AVIRIS image used in this study. Age classes 1, 3, 6 and 9 correspond to trees aged between 0 and 20, 41 and 60, 101 and 120, and >250 years respectively.

2. Wavelengths between 0.7 and 2.5 μm: the near and shortwave infrared light regions

In the region between 0.7 and 1.3 μm the reflectance of leaves is very high even though pigments and cell wall cellulose are transparent to light (Guyot and Riom, 1989). This can be attributed primarily to internal refraction at the cell wall boundaries caused by the difference in the index of refraction (n) between a hydrated cell wall (n = 1.47) and the index of refraction (n = 1.00) for air in the intercellular spaces (Grant, 1987). Since little absorption takes place, multiple refractions occur as the light encounters several layers of cell walls. This leads to high reflectance (Guyot and Riom, 1989). A small portion of the reflectance at these wavelengths can also be attributed to refraction at other interfaces in the leaf and to Rayleigh and Mie scattering within the leaf (Grant, 1987).

From 0.7 to 2.5 μm, many sharp absorption features appear due to light at certain wavelengths causing molecules or bonds within molecules to vibrate (Clark, 1999). The strongest vibrational absorptions are caused by water within the leaf. These vibrations are centred at 1.0, 1.45, 1.95, 2.0 and 2.2μm (Guyot and Riom, 1989; Green and Roberts, 1995). Additionally, vibrations related to organic molecules appear in the leaf spectra, and have been correlated to leaf chemicals such as lignin, nitrogen, chlorophyll, starch and various cations (Wessman, *et al.*, 1988; Johnson, *et al.*, 1994; Hallett, *et al.*, 1997). These absorptions have been attributed to overtones and combinations of vibrating C-H, O-H, N-H, C-C and C-N bonds in the 2.5 to 16μm region (Barton, *et al.*, 1992; Johnson, *et al.*, 1994).

1.2 Changes in canopy reflectance with stand age

As a stand ages, the canopy reflectance changes due to physiological and structural factors. Figure 1 shows the average reflectance of Douglas-fir stands of different ages obtained from an aircraft. This plot shows a general decrease in reflectance with stand age, although it should be noted that the values are not very precise due to differences in sun / sensor geometry and topography associated with the different stands.

Physiologically, the average age of exposed leaves on conifers tends to increase with tree age (Murtha, *et al.*, 1997). As leaves age, the reflectance in the visible range (0.4 to 0.7 μm) tends to decrease and the reflectance in the near infrared (0.7 to 1.4 μm) tends to decrease as well after a brief increase (Gates, 1965). The decrease in the visible range is due to an increase in pigment concentration with leaf age, causing greater absorption (Gates, 1965). As a juvenile leaf matures, there is an increase in near infrared reflectance due to the greater number of cell wall boundaries created by mesophyll development; immature leaves tend to have a very compact arrangement of cells in the mesophyll, whereas more mature leaves have more intercellular spaces (Grant, 1987). However, there is a decrease in reflectance with age after conifer needles mature. This decrease is most evident when comparing first and second year needles, and can be attributed to the mesophyll becoming denser (Guyot and Riom, 1989).

In the region near 0.7 μm there is a sharp increase in reflectance between the absorption centered at 0.645 μm caused by the chlorophyll and the high reflectance in the near infrared. The wavelength at which the reflectance increases the most rapidly is known as the red edge (Horler *et al.*, 1983) and it has been shown that the position of this absorption is correlated to leaf age in crop plants; as the leaf matures, the red edge shifts to progressively longer wavelengths (Collins, 1978). This is primarily related to the amount of chlorophyll in the leaf (Horler *et al.*, 1983). Care must be taken, since the wavelength of the red edge also reflects other variables such as species and stress (Horler *et al.*, 1983).

More subtle differences exist in the 0.7 to 2.5 μm range: the concentrations of certain leaf chemicals change as a tree matures, and these in turn affect the strength of the vibrational absorptions seen at these wavelengths. Zagolski *et al.* (1996) found that the concentration of nitrogen in maritime pine (*Pinus pinaster* Ait.) foliage decreased with age, whereas the concentrations of lignin and cellulose increased. These changes were most evident for younger stands.

The data presented in Figure 1 and analysed in this thesis were collected at the canopy, rather than the leaf level. For this reason, factors related to stand structure must be considered.

Leaf area index (LAI) is defined as the area of leaf over a given area of ground. In general, an increase in leaf area index causes the reflectance in the visible range to decrease due to the presence of pigments in the leaves and the reflectance in the near infrared range to increase due to within leaf refraction (Running, *et al.*, 1986). Long and Turner (1975) found that LAI increased in Douglas-fir before reaching an equilibrium value at about 40 years in planted stands and 60 years in natural stands.

Older forests also tend to have a greater variety of tree heights and a high number of gaps. This causes more shadowing to occur, causing a decrease in canopy reflectance at all wavelengths (Fiorella and Ripple, 1993).

1.3 Previous research

Several studies have previously examined the use of remotely sensed data for determining the ages of forest stands. DeWulf *et al.* (1990) attempted to use linear regression of multispectral and panchromatic SPOT-1 data to predict the ages of Corsican pine (*Pinus nigra* var. *maritima* Arnold) stands in Belgium. They found no significant correlation between the predicted ages and the test data. However, Danson (1987) found significant correlations between the ages of Corsican pine stands in northern England and the three multispectral SPOT-1 bands. Brockhaus and Khorram (1992) found significant

correlations between the ages of pine and hardwood stands in North Carolina and the digital numbers in Landsat TM bands 1 - 5 and 7. No significant correlation was found for the three SPOT-1 multispectral bands.

In recent years, several studies have applied more sophisticated techniques to determining the ages of forest stands in Oregon and British Columbia. Cohen and Spies (1992) used SPOT panchromatic and Landsat TM data which had been converted into the brightness, greenness and wetness tasseled cap components. They used linear regression models to estimate stand age in Oregon using these data as well as textural measurements obtained from the SPOT and transformed Landsat TM data. A high correlation was found between the SPOT texture and the stand age, as well as between the Landsat TM tasseled cap images and the ages of the stands.

Unsupervised classification using the brightness, greenness and wetness Landsat TM tasseled cap components, together with the amount of light incident on each pixel, was shown to yield a moderately high (78.3%) overall accuracy (Fiorella and Ripple, 1993). In this study in western Oregon, 99 classes were produced, and these classes were subsequently merged to yield five age classes: 0-10 years, 10-15 years, 20-90 years, 90-200 years and 200 or more years. The most confusion was between stands belonging to the 90 to 200 and 200 or more years age classes.

Cohen *et al.* (1996) modified the approach taken by Fiorella and Ripple (1993) to map forest ages. After converting the Landsat TM imagery into the brightness, greenness and wetness tasseled cap components, they used an unsupervised classification together with elevation data to identify areas with closed conifer canopies and to classify the remaining areas. For the closed conifer canopies, regression analysis was used based on the tasseled cap components and, in some trials, the sun incidence angle. This regression, together with a statistical model the authors developed, were used to classify the trees into either two (<= 200 years and >200 years) or three (<80 years, 80-200 years, >200 years) classes with respective accuracies of up to 81.1 and 73.6%.

In British Columbia, Niemann (1995) used Compact Airborne Spectrographic Imager (CASI) data in an attempt to classify stands on Vancouver Island into five age classes: 1 to 20 years, 21 to 40 years, 41 to 60 years, 81 to 100 years and >250 years corresponding the BC Ministry of Forest's age classes 1, 2, 3, 5 and 9. This study took two approaches to assess the separability of the classes. The first approach was to average bands together and create three ratios (green to red, red to near infrared and the normalized difference vegetation index). These ratios were used in a discriminant analysis. A 61% overall separability was found using the green to red and red to near infrared ratios, and a 65% separability was found using all three. There was a considerable amount of confusion among age classes 4, 5 and 9. Consequently a much higher separability was achieved when classes 4, 5 and 9 were aggregated into a single class. The second approach was to assess whether the wavelength of the red edge could be used to discriminate among the classes. Unfortunately a significant shift was not evident in the data.

Most recently, neural networks were used by Kimes *et al.* (1996) to determine the ages of young (age <50 years) stands in western Oregon. The neural network approach attempts to approximate the way in which neurons in a mammalian brain function. This method will be discussed more fully in the next section. For this research, data from Landsat TM bands 3, 4 and 5 were combined with data on the slope, aspect and elevation. The results were significantly better than the results from previous studies using more traditional linear techniques, and for the test data an RMS error of 5.68 years ($r^2 = 0.69$) was achieved.

1.4 Artificial neural networks

Using neural networks to process remotely sensed images is a fairly new approach which has become popular over the past ten years. The most common type of neural network is the feed-forward neural network, which is based on the work of Rumelhart *et al.* (1986). Feed-forward networks consist of a series of nodes arranged into three types of layers: the input layer, the hidden layer or layers and the output layer (see Figure 2). The nodes in each layer are connected to the nodes in the subsequent layers, and the connections have weights associated with them. In a traditional neural network classification, there is one input node associated with each band in the image, one or two hidden layers, and one output node for each desired output value (see Figure 2). When a pixel is processed, the digital number (DN) values of that pixel are normalised and become the values of the input nodes. These values are then passed to the nodes in the hidden layer connected to the input nodes. However, rather than being passed directly, they are first multiplied by the weight associated with the connections between the nodes. The receiving nodes then apply a sigmoid function to the sum of values they receive, and the results are passed to the nodes in either a second hidden layer or in the output layer. The end result is to have a value associated with each output node.

In order to set the weights associated with the connections, it is necessary to train the network prior to performing the classification. Initially the weights assigned to each connection are set to random values. The weights are then adjusted based upon the training data by undergoing many iterations of a training function, such as the generalized delta rule (Atkinson and Tatnall, 1997). The generalized delta rule can be expressed as:

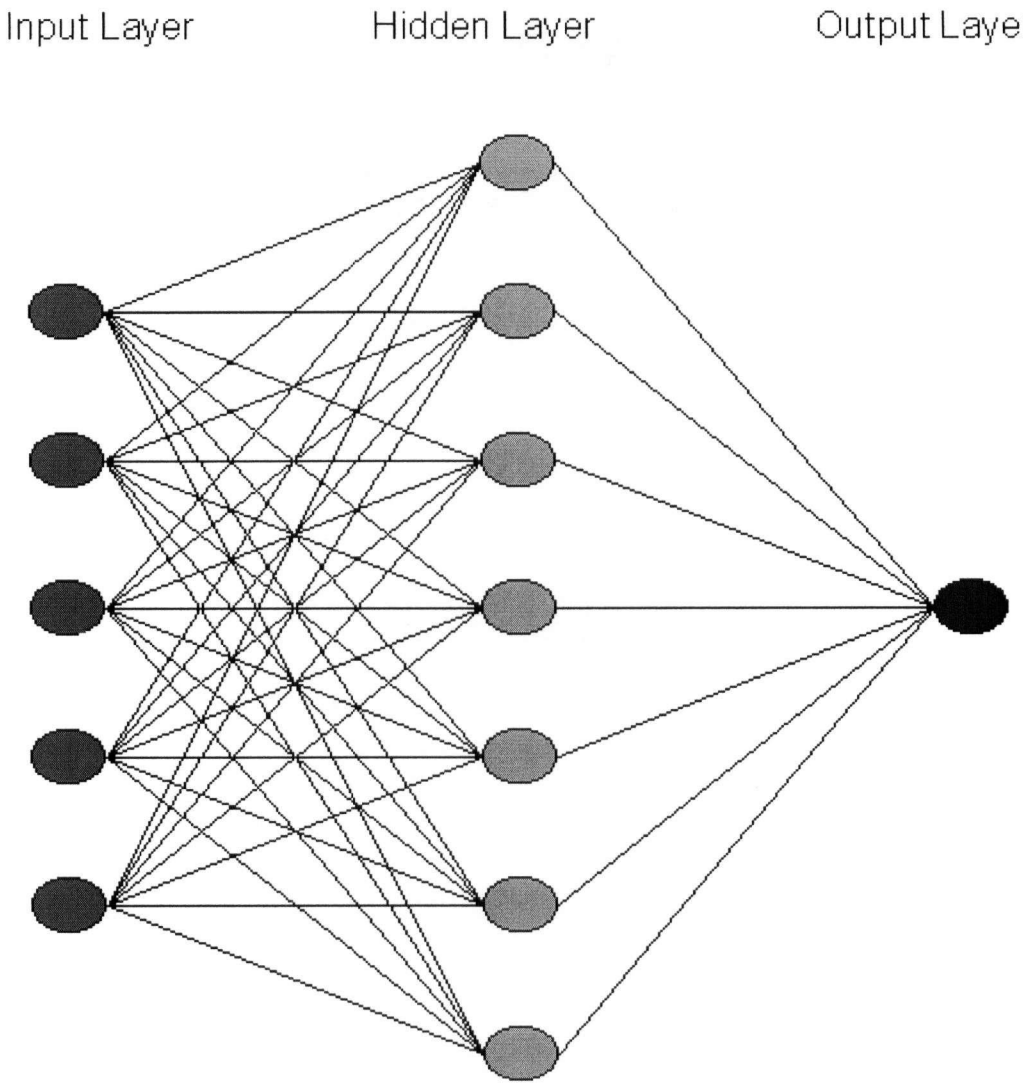

Figure 2: A typical artificial neural network
A diagram showing the structure of a typical artificial neural network with a single hidden layer. Neurons are depicted as ovals and connections between neurons are indicated by lines.

$$\Delta\omega_{ji}(\nu+1) = \eta(\delta_j o_i) + \alpha\Delta\omega_{ji}(\nu)$$

where:

$\Delta\omega_{ji}(\nu+1)$ is the change in the weight between nodes j and i

η is the learning rate parameter

δ_j is an index corresponding to the rate of change of the error

o_j is the output from node i

α is an optional momentum parameter

$\Delta\omega_{ji}(\nu)$ is the change in weight between nodes j and i for the previous iteration.

Neural networks have several advantages over traditional methods used for extracting information from images, and several of the advantages make them especially suitable for determining stand ages. Unlike conventional statistical methods, neural networks do not require that the inputs and outputs have a linear or simple non-linear relationship. Also, given sufficient training data, they are tolerant of errors in the training data. A third advantage is that many traditional models require the researcher to have some knowledge of the often complex relationships between the input and output data, whereas neural networks do not (Kimes *et al.*, 1998; Atkinson and Tatnall, 1997).

The spectral signatures of the individual stands will vary depending on the site quality, stand treatments, topography, the species present as well as many other factors. Interactions among these factors are quite complex, and may not be adequately addressed by a traditional statistical approach or well understood by the researcher creating the model. The tolerance to error is important in age studies, since in many cases the reference data have been collected by interpreting aerial photographs which is an error-prone technique.

1.5 Objective of study

The object of this study is to determine the age classes of forest stands on southern Vancouver Island. In this study a neural network approach was used in conjunction with data collected with the Airborne Visible / Infra-Red Imaging Spectrometer (AVIRIS). The AVIRIS instrument is an aircraft-mounted sensor which has 224 bands covering the 0.4 to 2.5 μm wavelength region at approximately 10 nm intervals (see Appendix 1). Typically this sensor is flown aboard a NASA ER-2 aircraft at an altitude of 20 km, producing data with a spatial resolution of 20 m and a swath width of 11 km (Green *et al.*, 1998). Because the spectral resolution is much higher than that of more traditional sensors such as Landsat TM and MSS and SPOT HRV and HRVIR, much more subtle spectral features, such as vibrational features related to canopy chemistry, can be detected. Attempts have previously been made to use high spectral resolution data to map stand ages, but in these studies only a fraction of the bands were used or the bands were averaged (e.g., Niemann (1995) and Holopainen (1998)).

Although no studies have yet been conducted on using neural networks to predict stand ages in hyperspectral data, several studies have used neural networks to process data with many bands. Yang *et al.* (1999) used neural networks to accurately predict mineral abundances using 40 AVIRIS bands. Bosch (1996) classified land cover using 22 visible and near-infrared bands, and Gong *et al.* (1997) used data from a field spectrometer sensitive to 226 wavelengths to identify tree species.

1.6 Study site and available data

The study site consists of the Sooke watershed portion of the Greater Victoria Water District (see Figure 3), which is approximately 30 km northwest of Victoria, British Columbia, Canada. This area covers 2033 ha, and consists primarily of Douglas-fir stands. Other species present include western red-cedar (*Thuja plicata* D. Don.) and western hemlock (*Tsuga heterophylla* Sarg.). The age classes present (see Tables 1a and 1b) reflect the active logging which has taken place in the past and continues today.

Data available for the study site includes photo-interpreted forest cover data on the primary and secondary species present and the ages of the stands. These data were originally collected at a scale of 1:20,000 and were later digitized and stored in a vector format. Additionally contour data (interval = 10 m) and a map showing road locations are available. AVIRIS imagery of the area was acquired on September 1, 1993 (Figure 4).

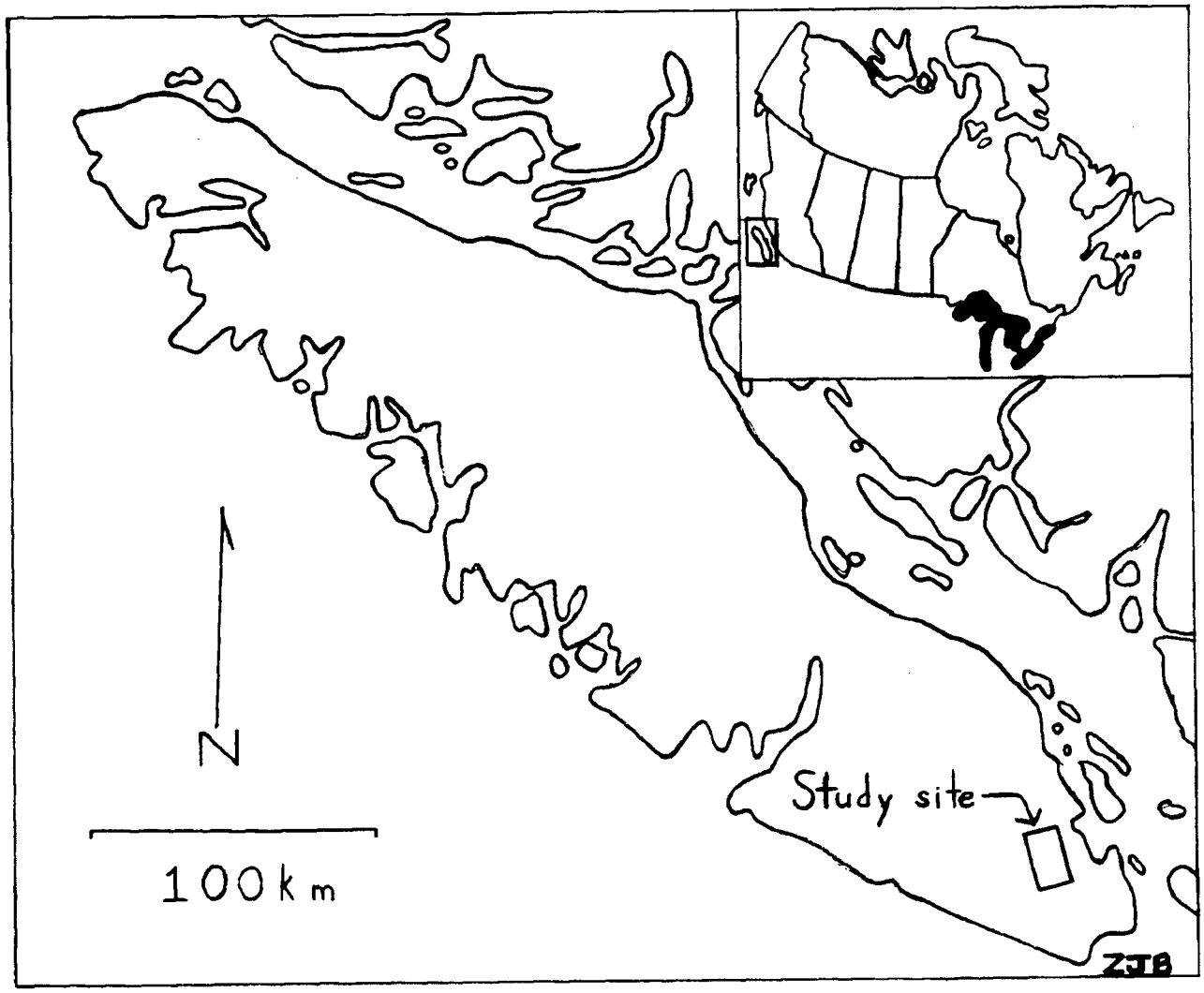

Figure 3: Location of the study site

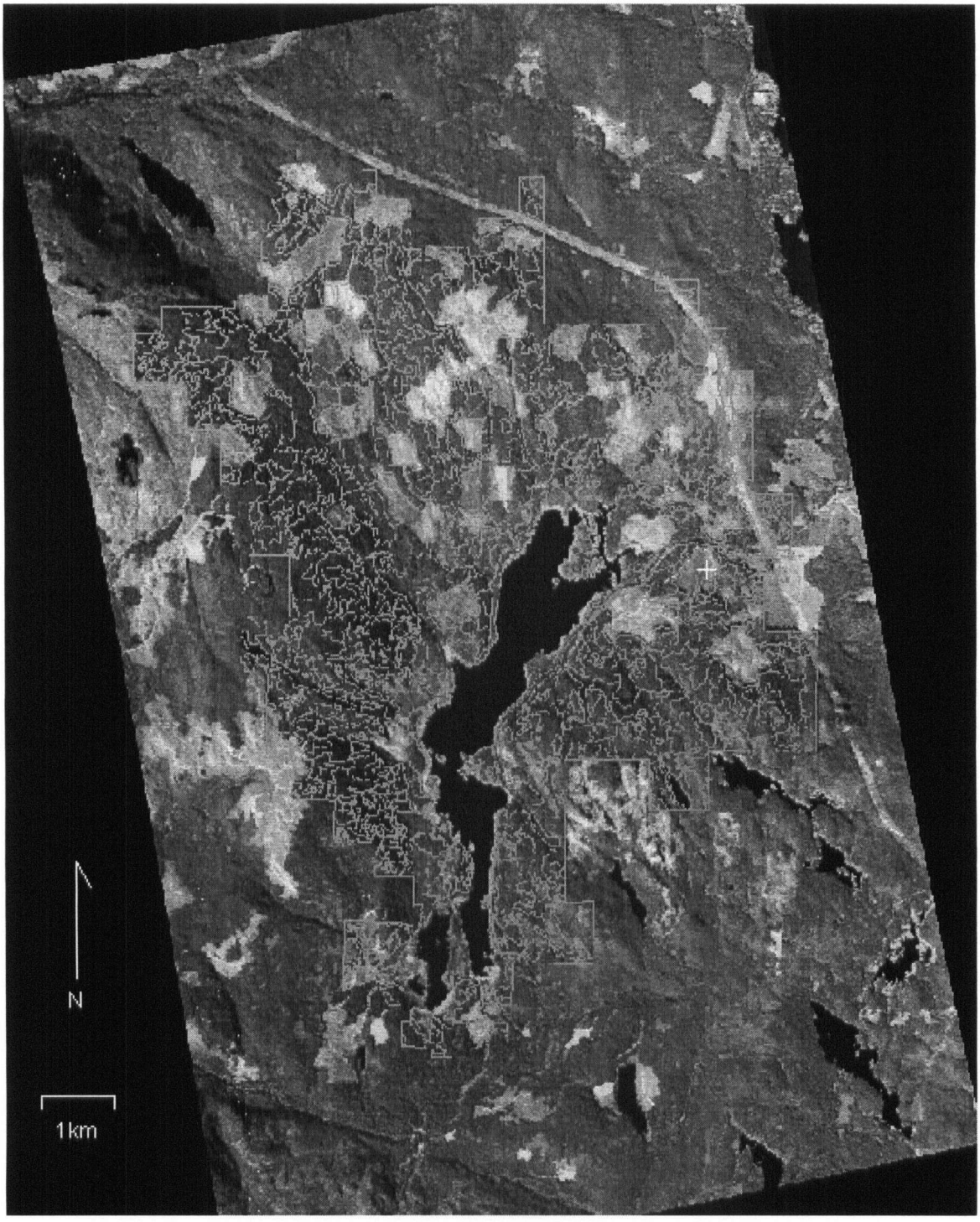

Figure 4: The AVIRIS scene
A false colour composite showing the AVIRIS scene. The forest cover polygon boundaries are indicated by gray lines.

Douglas-fir only			
Age Class	Number of Polygons		
	All polygons	>10,000 m^2	>40,000 m^2
1 (0 - 20 years)	27	22	14
2 (21 - 40 years)	66	57	35
3 (41 to 60 years)	10	8	6
4 (61 - 80 years)	20	15	4
5 (81 - 100 years)	43	29	13
6 (101 - 120 years)	16	14	7
8 (141 - 250 years)	255	226	119
9 (>250 years)	10	9	8

Table 1a: Attributes of pure Douglas-fir stands

All species			
Age Class	Number of Polygons		
	All polygons	>10,000 m^2	>40,000 m^2
1 (0 - 20 years)	94	76	54
2 (21 - 40 years)	118	102	55
3 (41 to 60 years)	26	21	12
4 (61 - 80 years)	36	29	10
5 (81 - 100 years)	84	67	29
6 (101 - 120 years)	54	47	24
8 (141 - 250 years)	424	375	195
9 (>250 years)	12	11	10

Table 1b: Attributes of all stands

Note that both tables include columns indicating the number of polygons where polygons of all sizes are included. Also included are the number of polygons meeting minimum size requirements: >10,000 m^2 and >40,000 m^2.

CHAPTER II: Method

2.1 Image preparation

The AVIRIS imagery of the study area originally consisted of two 614 x 512 images in 16 bit unsigned integer format. In order to facilitate image processing, the two images were joined and the byte order switched from big-endian to little-endian in order to facilitate image processing on an Intel x86-based machine.

Next, the image was converted from at-sensor radiance to reflectance using version 3.0 of the Atmosphere Removal (ATREM) software (Gao *et al.*, 1997). It was important to convert the image to reflectance because the atmospheric effects could vary over the image, and because it is necessary to know the reflectance in order to convert the image to absorption and produce a first difference image (please see below).

The ATREM program models the effects of the atmosphere using the Simulation of the Satellite Signal in the Solar Spectrum (5S) radiative transfer model. This model can be used to show that the surface reflectance (ρ) can be estimated using the following equation (Gao *et al.*, 1997):

$$\rho(\lambda) = \frac{(\frac{\rho^*(\theta_s,\phi_s,\theta_v,\phi_v,\lambda)}{T_g(\theta_s,\theta_v,\lambda)} - \rho_a(\theta_s,\phi_s,\theta_v,\phi_v,\lambda)}{T(\theta_s,\lambda)T(\theta_v,\lambda) + S(\lambda)(\frac{\rho^*(\theta_s,\phi_s,\theta_v,\phi_v,\lambda)}{T_g(\theta_s,\theta_v,\lambda)} - \rho_a(\theta_s,\phi_s,\theta_v,\phi_v,\lambda)}$$

where:
θ_s is the solar zenith angle
ϕ_s is the solar azimuth angle
θ_v is the sensor zenith angle
ϕ_v is the sensor azimuth angle
λ is the wavelength
r is the surface reflectance
ρ^* is the apparent reflectance, which is defined by the equation:

$$\rho^*(\theta_s,\phi_s,\theta_v,\phi_v,\lambda) = \frac{\pi L(\theta_s,\phi_s,\theta_v,\phi_v,\lambda)}{\mu_s E_s(\lambda)}$$

where:

L is the at sensor radiance (the flux of electro-magnetic energy received per unit area per unit wavelength)
μ_s is the equal to cos θ_s
E_s is the flux of light from the sun which is incident on the top of the atmosphere

$T(\theta_s)$ is the downward scattering transmittance
$T(\theta_v)$ is the upward scattering transmittance
T_g is the transmission of the gasses in the sun-surface-sensor path, which is equal to the product of the transmissions of the individual gasses.
S is the spherical albedo of the atmosphere

These terms are calculated from different sources. The at sensor radiance (L) is obtained from the digital numbers in the image, since they are directly related.

The solar zenith and azimuth angles, θ_s and ϕ_s, and the flux of light from the sun incident on the top of the atmosphere (E_s) are based on the date, time of day and location in conjunction with a solar almanac.

The upward and downward scattering transmittances and the spherical albedo are calculated using the ground visibility and knowledge of the aerosol type in the study area. Unfortunately, the ground visibility was not collected at the study site at the time of data acquisition. Therefore visibility data collected at the Victoria International Airport (approximately 35 km from the study site) were used instead. A marine aerosol model was chosen due to the site's proximity to the ocean.

The transmissions of the individual gases, T_g, were determined in two different ways. Since the absorption due to ozone, CO_2, N_2O, CO, CH_4, and O_2 do not vary significantly, a single transmission value could be used over the entire image. This value could be computed with a model which considered geography (in this case mid-latitude summer), and the solar and sensor geometry.

Water vapor does vary significantly over the image, so for each pixel the transmission of the water vapor was calculated. This was done by determining the amount of water vapor present by calculating the depths of the 0.94 and 1.14μm water absorption features. Calculations were made by examining the ratios of the DN values in bands centered on and surrounding the wavelength of the absorptions.

2.2 Georeferencing the AVIRIS data

The data giving information on the species composition and ages of the stands in the study area, as well as the topographic data, came referenced to the Universal Transverse Mercator (UTM) coordinate system. Since the AVIRIS data were not georeferenced, it was necessary to rectify the data so that it would match the forest cover

and contour data. Unfortunately, this was a somewhat difficult problem, since the image was distorted by flight irregularities (pitch, roll and altitude changes) during image acquisition (Figure 5). Additionally, topographic differences within the image added to the difficulty since it meant that the spatial dimensions of each pixel were variable. An attempt was made to correct for the flight irregularities using the method described by Clark *et al.* (1998). However, it was found that this process did not improve the image quality so it was not used. Instead, a simple second order transformation was used on the original image (Richards and Jia, 1999; pp. 56-63). This transformation can be described by the equations:

$$u = a_0 + a_1 x + a_2 y + a_3 xy + a_4 x^2 + a_5 y^2$$
$$v = b_0 + b_1 x + b_2 y + b_3 xy + b_4 x^2 + b_5 y^2$$

where u and v are the coordinates of the pixels in the image, and x and y are the coordinates of the pixels on the map. a_n and b_n are coefficients set by finding the least squares solutions to the two equations, based on a series of corresponding points in the image and road map. Values in the new image grid were assigned by using the nearest neighbour method. This method can be thought of as overlapping the pixels in the corrected image with the pixels in the original image. Since the pixels in the corrected image and the pixels in the original image do not line up perfectly, each pixel in the corrected image contains portions of several pixels from the original image. The value assigned to a corrected pixel is the value of the pixel in the original image comprising the greatest proportion of the corrected pixel. This method was used because it did not alter the original pixel values by averaging pixels.

For the image being corrected in this study, 94 corresponding points (ground control points) were located, giving an RMS error of 2.04 pixels in the X direction and 1.87 pixels in the Y direction.

It would have been possible to use a higher order correction in an attempt to obtain a more accurate registration. This was not done for two reasons. First there were obvious mistakes present in the road map of the area, and a lower order correction was better able to average out errors. The other reason is that there were areas of the image in which it was difficult to collect ground control points. When higher order corrections are used, errors tend to propagate more quickly than when a second order correction is chosen, due to the greater number of degrees of freedom.

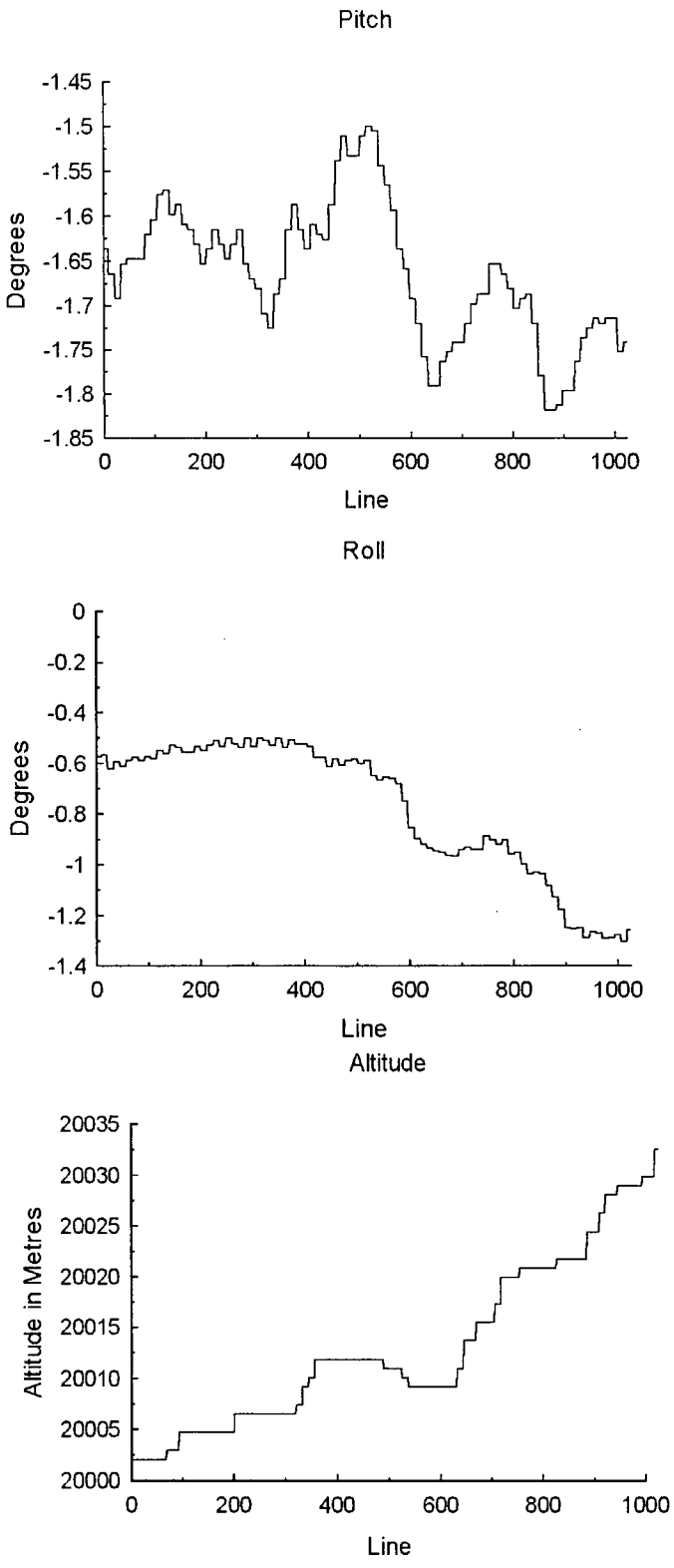

Figure 5: Pitch, roll and altitude during the AVIRIS image acquisition

2.3 Rasterizing the forest cover data

Two raster images were created from the vector forest cover map using the PCI EASI/Pace module GRDPOL. The first contained the age classes for pure Douglas-fir stands, and the second contained the age classes for all forested areas regardless of the species present. The raster data were produced in such a way that they would have the same dimensions and pixel size as the AVIRIS image so that the pixels would overlay one another.

2.4 Creating topographic and view angle data

Previous research has shown that terrain orientation and slope have a significant impact on the amount of light reflected from a canopy which reaches a sensor (Fiorella and Ripple, 1993). Additionally, Kimes *et al.* (1996) found that neural networks were able to effectively integrate remotely sensed data with topographic data in order to produce more accurate age estimates. Therefore, slope and aspect images were created from the contour data using the Idrisi module SURFACE. These images had the same dimensions as the AVIRIS data and were appended to them.

When the AVIRIS image was visually inspected, it was discovered that pixels on the west side of the image were darker than those on the east side. This is most likely due to the fact that natural surfaces do not reflect light equally in all directions (they are non-Lambertian). The amount of light is dependant on the zenith angle of the sun and the view angle of the sensor (Guyot and Riom, 1989). In an attempt to address this, a program was written to calculate the view angle associated with each pixel. Positive and negative values were used to indicate the direction. The output from this program was appended to the AVIRIS data.

2.5 Eliminating noisy bands

It was observed that bands which contained strong atmospheric absorptions or in which some objects had very low reflectance were noisy or had calculated reflectance values which were negative. Therefore the bands were visually inspected, and bands which appeared noisy were eliminated. Bands eliminated in this way were bands 1 to 15, 33, 97, 107 to 116, 153 to 170, 174 and 215 - 224.

2.6 Creating first difference images

To produce a first difference, the reflectance measurements obtained using ATREM were converted to absorption using Beer's law, $a = \log (1/R)$, where a is absorption and R is the reflectance (Wessman *et al.*, 1988). The absorption measurements in adjacent channels were then subtracted from one another to produce a first difference image: $fd_i = a_{i+1} - a_i$, where fd_i is the calculated first difference value in

band i and a_i and a_{i+1} are the absorptions in bands i and i +1respectively. As a last step the values were scaled and stored as 16 bit unsigned integers.

Wessman *et al.* (1988) noted that using first difference images helps eliminate confusion among adjacent vibrational absorptions, and helps eliminate baseline shifts in the spectra. In this case, the baseline shifts were due to the non-Lambertian surface reflectance and topography.

2.7 Creating the training data

A program was created to systematically create the training data for stands containing only Douglas-fir and for stands containing all species. This was done in order to minimize operator bias and spatial autocorrelation.

Training sets were created for the reflectance data with and without the topographic and view angle information, and for the first difference data. Topographic and view angle data were not included since creating a first difference image should correct for the illumination differences. A training set was produced which averaged bands together in order to simulate Landsat TM bands 2 to 5 and 7 (the AVIRIS bands corresponding to Landsat TM band 1 were considered to be noisy) together with the topographic and view angle data. This data set was created in order to assess what advantage, if any, exist in using hyperspectral rather than conventional multispectral data. A final data set consisted of the non-noisy bands <1.0 μm (51 bands) together with the topographic and view angle data. The reasons for creating this set were twofold. First it reduced the number of bands, reducing the likelihood of overfitting the data. Secondly most of the age-related spectral changes discussed earlier occur in this wavelength region.

Each training set consisted of 100 samples of each age class present (for a total of 800 samples.) This training set is considerably smaller than the one used by Kimes *et al.* (1996), which had 6593 samples. It was felt that such a large training set would be impractical in operational forestry. There are several guidelines available regarding the minimum sample size required to reduce the amount of overfitting to an acceptable level. For instance Masters (1993; p. 248) suggests that the minimum number of samples should be at least twice the number of connections in the network being used. Despite these guidelines, data with many bands and very few training samples have been successfully processed in the past (e.g., Gong, *et al.* (1997)).

The process for collecting the data set was as follows:

1. Determine the number of pixels belonging to age class 1, eliminating pixels which were within two pixels of a pixel belonging to another age class or the image boundary. Eliminating these pixels was done to help compensate for the misregistration between the age class map and the AVIRIS image.
2. Divide the number of pixels from step 1 by 100 to determine the sampling interval, and systematically identify the pixels to be included in the training set.

3. Write the image, topography and view-angle data corresponding to the samples which were identified to a text file.
4. Repeat steps 1 to 3 for the remaining age classes.

2.8 Processing the data

The training data were then input into the QwikNet artificial neural network simulation program (Jensen, 1999) and several architectures were evaluated (Table 5). Some authorities suggest using networks with a greater number of hidden nodes than were used in this study, but all these studies involve performing image classification rather than obtaining a single vegetation parameter. Kanellopoulos and Wilkinson (1997), for instance, suggest that the hidden layer or first hidden layer in a two hidden layer system should have two to three times the number of input bands. In hyperspectral classification, Yang *et al.* (1999) used 40 hidden nodes arranged in a single layer (input bands = 40, output classes = 15). Bosch (1996) tried using between 14 and 22 hidden nodes in a single layer and using a two hidden layer model with between 15 and 22 nodes in the first hidden layer and between 14 and 21 in the second (input bands = 23, output classes = 14 or 4).

Smaller numbers of hidden nodes were chosen for this study for two reasons. First using fewer nodes minimizes the number of connections and therefore reduces the network's tendency to overfit the dataset. Secondly, the studies cited involved performing classifications. In a classification, several output nodes are required instead of one output node as in this study, and each output class may consist of two or more non-contiguous spectral regions which need to be merged to form a single class. (Kanellopoulos and Wilkinson, 1997) This means that a much larger set of relationships needs to be analysed by the network than in the current study, which necessitates a larger number of hidden nodes.

Each network was trained for 10,000 epochs using the generalized delta rule with a learning rate of 0.1 or 0.2. These learning rates were chosen in order to examine the effect of the learning rate on the accuracy of the prediction. Choosing a starting learning rate of 0.1 is consistent with previous neural network studies involving hyperspectral data including Yang *et al.* (1999) and Bosch (1996). Additionally, the architecture and training parameters found to be optimal by Gong *et al.* (1997) in their analysis of spectrometer data for tree species identification were used (50 hidden nodes, learning rate = 0.3, momentum = 0.7).

A logistic activation function,

$$y = \frac{1}{1 + e^{-x}}$$

Hidden Layers	Hidden Nodes	Learning Rates
1	3	0.1 and 0.2
1	4	0.1 and 0.2
1	5	0.1 and 0.2
1	10	0.1 and 0.2
1	20	0.1 and 0.2
2	10 and 5	0.1 and 0.2
2	50	0.3

Table 2: **Neural network architectures and training parameters used in this study** The architecture having fifty hidden nodes was only used on the dataset containing the reflectance, view angle and topographic data for the pure Douglas-fir stands. The learning rate of 0.2 was also only used on this dataset.

where x is the sum of the inputs to the node and y is the node's output was used. A logistic function is the most common activation function, and the choice of functions usually has very little impact on the performance of a network. (Masters, 1993; p. 81)

After the networks had been trained, the neural networks were used to predict the age classes of all forested pixels in the image. Once this had been done, the pixel values were combined in one of two ways to assign predicted ages to the forest cover polygons. The first way was to covert the predicted age classes to integers by rounding (the neural network produced decimal numbers as output) and then to choose the most frequent age class. The second way was to simply average the values.

From a statistical standpoint, averaging the values raises two important issues. First, the results will be continuous real numbers (e.g. an age class of 2.7) whereas age classes are integers, where each integer represents a range of ages. This means that technically there cannot be an age class of 2.7. However, the age class of 2.7 can be interpreted as indicating that the data values show that the polygon belongs to either age class 2 or age class 3, but that it more closely resembles age class 3. This could potentially be useful information for people using the data who are concerned with the accuracy of the predictions.

Secondly, age classes correspond to different age increments. For instance, age class 1 corresponds to a 20 year increment whereas age class 8 corresponds to a 110 year increment. This means that there is not a linear correspondence between the age class numbers and the ages the numbers represent. However, this may not be an issue when using neural networks. The age classes were treated by the network as a linear set of numbers during training, and the input data were non-linearly combined in a way that fit the age classes. Additionally, many of the changes which take place as a stand ages, such as changes in LAI and leaf chemistry are highly non-linear with respect to age.

The root mean square (RMS) error and Spearman's correlation coefficients (r_s) were calculated for each trial. The formula used for the RMS calculation was:

$$RMS = \sqrt{\frac{\sum (X-Y)^2}{n}}$$

where X and Y are vectors corresponding to the actual and predicted age classes of the polygons respectively, and n is the number of polygons. This statistic indicates the errors associated with the predicted age classes in terms of fractions of age classes.

The correlation coefficient is a number between -1 and 1 which indicates the correlation between two vectors. A value of zero indicates no linear correlation, and values of 1 and -1 indicates perfect correlation and anticorrelation respectively. The value is not affected by the unit of measurement (Davis, 1986; p. 38). In most remote

sensing studies, the Pearson method is used to calculate the correlation. Unfortunately this statistic assumes that the vectors being compared are normally distributed about their means (Ott, 1993; pp. 465). From Table 1 we can see that the distributions of the age classes are skewed, which may affect the validity of this statistic.

An alternative to the Pearson method is to use the Spearman method to calculate the correlation coefficient (Ott, 1993; pp. 465). The Spearman method does not require that the data being compared are normally distributed, which makes it suitable for the data in this study.

Calculating the correlation coefficient using the Spearman method is a two step process. The first step is to individually calculate the rank for the two data vectors being compared. Next the correlation coefficient is calculated using the formula:

$$r_s = \frac{n(\sum X_r Y_r) - (\sum X_r)(\sum Y_r)}{\sqrt{[n\sum X_r^2 - (\sum X_r)^2][n\sum Y_r^2 - (\sum Y_r)^2]}}$$

where:

r_s is the correlation coefficient calculated using the Spearman method
n is the number of samples in the population
X_r and Y_r are the two vectors containing the ranks of the original datapoints

The final step was to perform a one-tailed test to determine if the degree of correlation observed was significant at the $\alpha = 0.05$ level. These statistics were calculated for polygons >10,000 m^2 and for polygons >40,000 m^2 in order to examine the effect of polygon size on the prediction accuracy. The choice of 10,000 and 40,000 m^2 was based on the presence of natural breaks in the data.

CHAPTER III: Results and discussion

The best stand age predictions produced using each of the different datasets are shown in Tables 2a and 2b. Appendices 2 and 3 show the full set of results. Tables 3a through 3c and 4a though 4c show the confusion matrices for the best results for the pure Douglas-fir polygons and for all polygons. Although none of the results meet the guidelines established by the BC Ministry of Forests for the Vegetation Resources Inventory (BC Ministry of Forests, 1998b), the results do show that age can be predicted with some accuracy using neural networks in conjunction with hyperspectral data. Additionally almost all correlations were significant at the $\alpha = 0.05$ level.

The best results show that an RMS error of 1.84 age classes ($r_s = 0.6708$) can be achieved when just the pure Douglas-fir stands are examined,. An RMS error of 1.94 age classes ($r_s = 0.6883$) can be achieved for all stands. Figures 6a and 6b show the best Douglas-fir only results, and Figures 7a and 7b show the best mixed species results. These results are especially encouraging since many of the stands in the study area belong to the older age classes, which others (e.g. Niemann, 1995) have had trouble separating from one another. A number of observations can be drawn from the two tables:

1. A higher correlation and a lower RMS error were observed when only larger polygons (with an area >10,000 or >40,000 m^2) were included. This is most likely due to two reasons. First, more pixels were examined to determine a polygon's age, since the larger polygons contained more pixels. This led to an averaging out of errors. Second, fewer pixels were located near the polygon edges, where pixels could belong to adjoining polygons due to image to map misregistration.

2. Consistent differences were not seen between different neural network architectures. This suggests that the patterns being identified by the neural networks were simple enough to be identified by a network with only three or four hidden nodes. Alternatively, the results could be interpreted as an indication that the problem of overfitting the data did not increase when a greater number of connections were present.

3. Both the RMS errors and the correlation coefficients were similar for the dataset (Douglas-fir only, reflectance data for all bands plus topographic and view angle data) which was trained with a learning rate of 0.1 and a learning rate of 0.2. This indicates that small changes in the learning rate do not cause a significant increase or decrease in accuracy.

4. Surprisingly, large differences in accuracy did not exist between the trials run on pure stands of Douglas-fir and the trials run on stands of all species. This may indicate that the species present (almost exclusively conifers) follow a similar spectral pattern as they mature. A possible implication is that it may be unnecessary to stratify based on species before performing this type of analysis.

Douglas-fir only

			All areas		Polygons >10,000 m²		Polygons >40,000 m²	
Dataset	**Hidden Nodes**	**Learning Rate**	**RMS Error**	**r_s**	**RMS Error**	**r_s**	**RMS Error**	**r_s**
Reflectance, topographic data, view-angle	4	0.1	1.84	0.67	1.72	0.71	1.38	0.80
Reflectance, topographic data, view-angle	10 and 5	0.2	1.97	0.64	1.82	0.70	1.51	0.79
Reflectance only	10 and 5	0.1	1.92	0.65	1.75	0.70	1.47	0.78
Visible / NIR, topographic data, view angle	10	0.1	2.03	0.65	1.79	0.68	1.54	0.77
Simulated Landsat TM	4	0.1	3.14	0.12	3.05	*0.08*	3.11	*0.07*
First Difference	4	0.1	2.09	0.62	1.96	0.66	1.74	0.75

All species

			All areas		Polygons >10,000 m²		Polygons >40,000 m²	
Dataset	**Hidden Nodes**	**Learning Rate**	**RMS Error**	**r_s**	**RMS Error**	**r_s**	**RMS Error**	**r_s**
Reflectance, topographic data, view-angle	10	0.1	2.07	0.66	1.89	0.70	1.58	0.80
Reflectance only	4	0.1	1.94	0.69	1.77	0.74	1.55	0.82
Visible / NIR, topographic data, view angle	4	0.1	2.19	0.64	2.11	0.67	1.86	0.77
Simulated Landsat TM	20	0.1	2.14	0.61	2.05	0.65	1.75	0.78
First Difference	4	0.1	2.20	0.63	2.11	0.66	1.93	0.76

Tables 3a and 3b: The best results for each training set.
The results in this table represent a subset of the results in Appendices II and III. Results were chosen based upon the lowest RMS error observed for each training set. All results are based on the mean predicted age per polygon, since this method of combining pixels gave the lowest RMS errors.

Douglas-fir only									
		Photo-interpreted age classes							
Predicted age classes		**1**	**2**	**3**	**4**	**5**	**6**	**8**	**9**
	1	0	1	0	0	1	0	0	0
	2	12	15	0	0	1	0	2	0
	3	3	27	5	5	2	1	8	0
	4	4	16	3	7	3	1	14	0
	5	2	5	1	2	8	4	21	1
	6	0	2	1	1	15	4	51	1
	7	1	0	0	4	12	6	111	2
	8	0	0	0	1	1	0	48	6
	9	0	0	0	0	0	0	0	0

Douglas-fir stands >10,000 m^2									
		Photo-interpreted age classes							
Predicted age classes		**1**	**2**	**3**	**4**	**5**	**6**	**8**	**9**
	1	0	0	0	0	0	0	0	0
	2	11	13	0	0	1	0	1	0
	3	8	25	3	5	2	1	3	0
	4	1	13	3	4	3	1	12	0
	5	1	4	1	2	5	3	19	0
	6	0	2	1	0	10	4	46	1
	7	0	0	0	3	7	5	101	2
	8	0	0	0	1	1	0	44	6
	9	0	0	0	0	0	0	0	0

Douglas-fir stands >40,000 m^2									
		Photo-interpreted age classes							
Predicted age classes		**1**	**2**	**3**	**4**	**5**	**6**	**8**	**9**
	1	0	0	0	0	0	0	0	0
	2	8	6	0	0	0	0	0	0
	3	0	19	3	1	1	0	0	0
	4	0	7	1	1	1	0	1	0
	5	0	3	1	2	2	1	8	0
	6	0	0	1	0	7	2	27	1
	7	0	0	0	0	2	4	57	2
	8	0	0	0	0	0	0	26	5
	9	0	0	0	0	0	0	0	0

Tables 4a, 4b and 4c: Confusion matrices for the pure Douglas-fir stands
The data used consists of the best pure Douglas-fir results. These results were produced using the reflectance image plus togography and view angle data. Four hidden nodes arranged in a single layer were used with a learning rate of 0.1.

All species

Predicted age classes \ Photo-interpreted age classes	1	2	3	4	5	6	8	9
1	14	6	0	1	1	0	3	1
2	39	30	2	2	0	0	3	0
3	25	40	4	1	5	0	12	0
4	12	27	10	8	8	5	22	0
5	3	9	6	9	18	17	58	0
6	0	5	4	10	34	22	127	3
7	1	1	0	5	17	8	184	7
8	0	0	0	0	1	2	15	1
9	0	0	0	0	0	0	0	0

All Stands >10,000 m²

Predicted age classes \ Photo-interpreted age classes	1	2	3	4	5	6	8	9
1	10	3	0	0	0	0	0	0
2	36	25	0	2	0	0	1	0
3	22	38	4	1	3	0	7	0
4	6	23	10	7	6	4	17	0
5	1	8	6	8	16	14	51	0
6	0	4	1	8	29	20	116	3
7	0	1	0	3	12	8	170	7
8	0	0	0	0	1	1	13	1
9	0	0	0	0	0	0	0	0

All Stands >40,000 m²

Predicted age classes \ Photo-interpreted age classes	1	2	3	4	5	6	8	9
1	10	0	0	0	0	0	0	0
2	29	12	0	0	0	0	0	0
3	14	26	3	0	1	0	1	0
4	1	16	6	3	0	0	5	0
5	0	1	3	4	8	6	21	0
6	0	0	0	3	15	12	67	3
7	0	0	0	0	5	5	98	5
8	0	0	0	0	0	1	3	1
9	0	0	0	0	0	0	0	0

Tables 5a, 5b and 5c: Confusion matrices for all stands in the study area
The data used consists of the best results for all stands in the study area regardless of species. The results were produced using the reflectance data without topographic or view-angle data were used in the analysis. Four hidden nodes arranged in a single layer were used with a learning rate of 0.1.

Known Age Classes: Douglas-fir Only

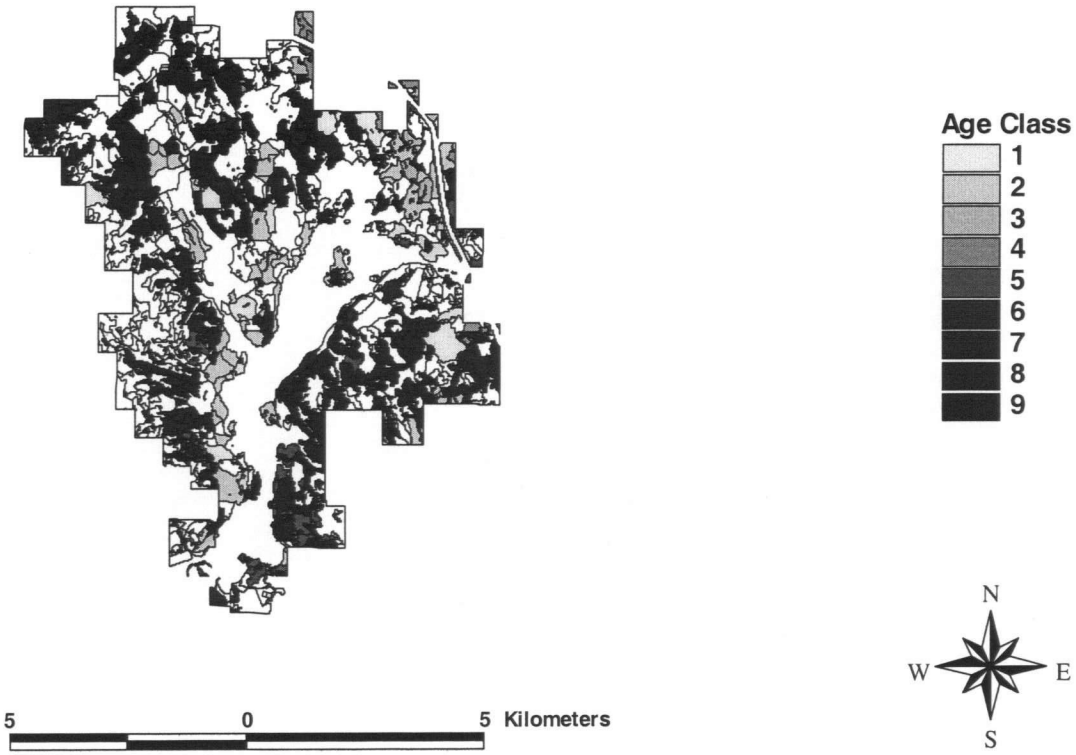

Figure 6a: **Photo-interpreted stand ages for pure Douglas-fir stands in the study area**

Predicted Age Classes: Douglas-fir Only

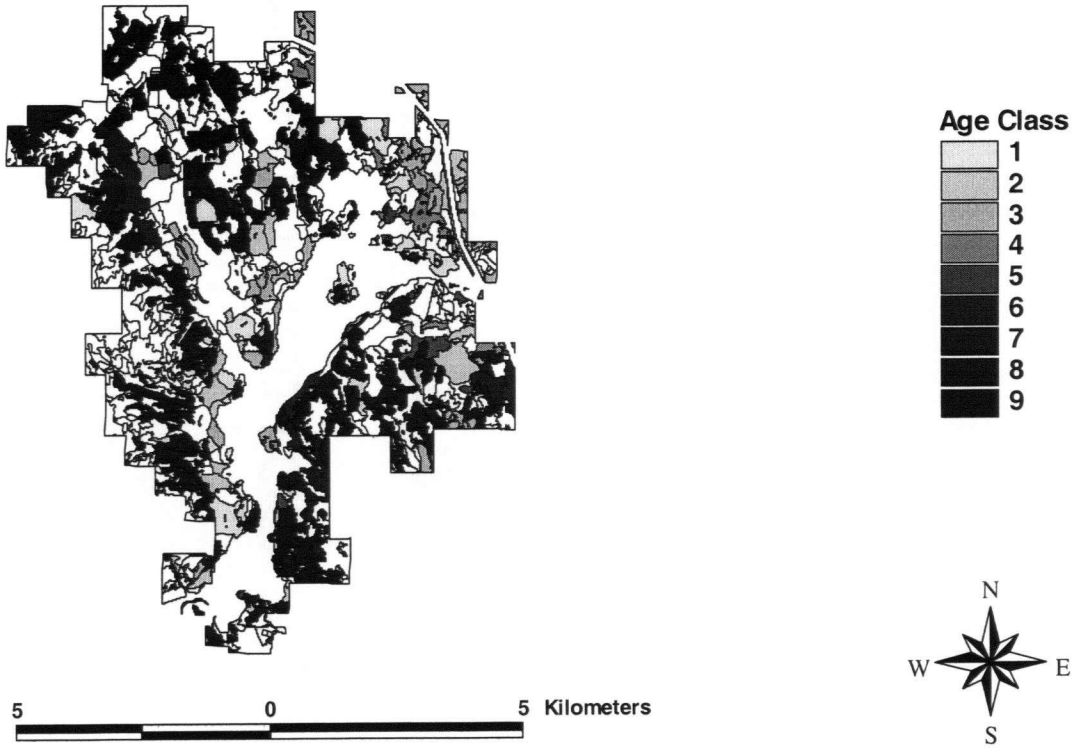

Figure 6b:Ages determined for pure Douglas-fir stands using an artificial neural network
The data used consisted of the reflectance image plus togography and view angle data. Four hidden nodes arranged in a single layer were used with a learning rate of 0.1.

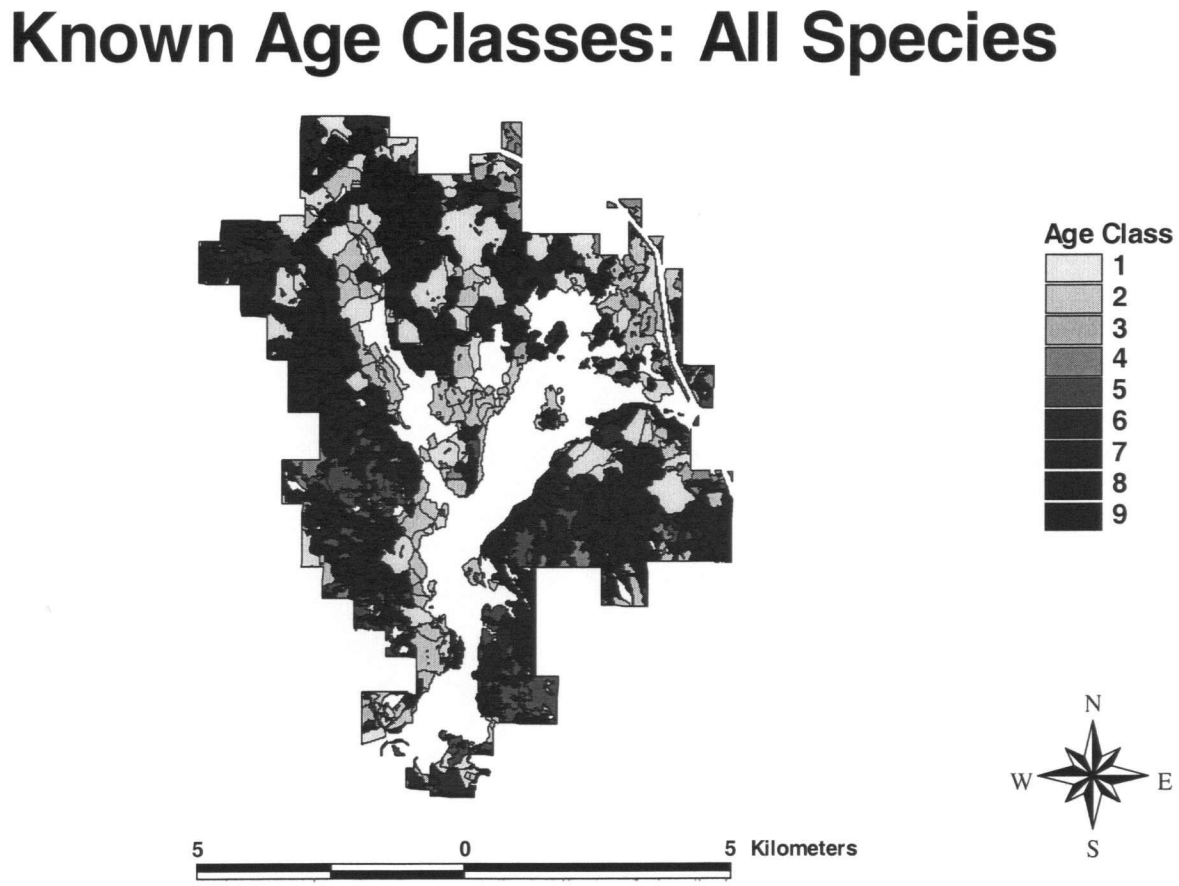

Figure 7a: Photo-interpreted stand ages for all stands in the study area

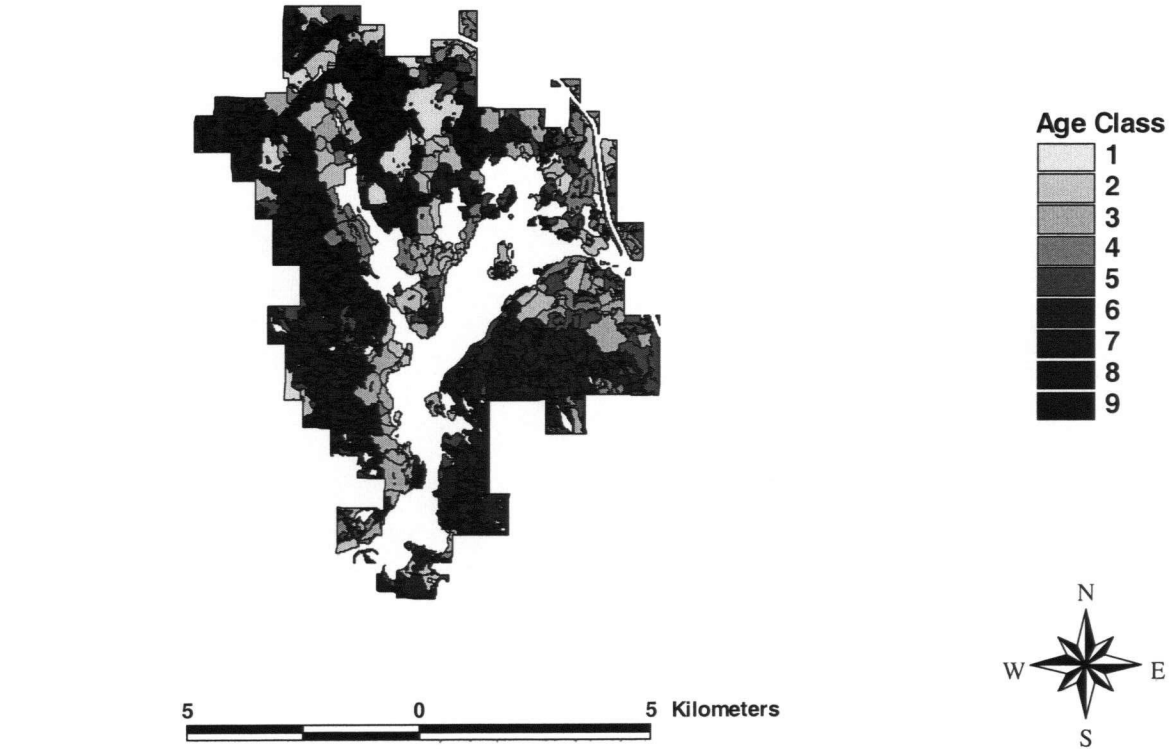

Figure 7b: **Ages determined for all stands using an artificial neural network**
The reflectance data without topographic or view-angle data were used in the analysis. Four hidden nodes arranged in a single layer were used with a learning rate of 0.1.

5. For the data consisting of all polygons regardless of species, the accuracy of the classification using the reflectance in all bands (but not the topographic or view angle data) was higher than the accuracy using reflectance plus the topographic and view angle data. Two possible explanations exist. First, the data contained in the additional fields may not have been useful in the analysis and the additional data increased the number of connections causing more overfitting. Alternatively, the topographic data may have allowed the network to learn the location of the training sites, since most training samples would be taken from the centres of the larger polygons. This would be problematic when small polygons were included during the processing and error analysis phases, since the locations would be different. The decrease in accuracy was not seen for the pure Douglas-fir stands.

6. In nearly all cases there was a lower correlation and a higher RMS error when the frequency method was used to combine pixels within a polygon than when the averaging technique was used. This error may be due in part to the rounding associated with the frequency method, or with roads within the polygons. Roads might affect the frequency since all the road pixels within a polygon would probably be assigned age class 1. Therefore even though the roads might constitute a small fraction of the area of a polygon, because the variance of the road pixels is so low age class 1 might be the most frequent class in the image. Interestingly the difference between the frequency and averaging methods was largest for the data sets containing the full set of bands, and smallest for the dataset simulating the Landsat TM data for all species. The reason for this is not known.

7. The results from the simulated Landsat TM image together with topographic and view angle data for the mixed species data were comparable to results using more bands when the averaging technique was used to combine pixels, and better when the frequency technique was used. This suggests that using hyperspectral data may not add to the accuracy of the age prediction, although it would be useful to see if this is still the case when a larger training set is used. The results from the simulated Landsat TM data for the pure Douglas-fir stands were poor. The most likely explanation is that a processing error occurred, although the process was repeated twice with similarly poor result.

8. First difference spectra produced equivalent or slightly worse results than the reflectance data. This may be due to image noise, since when adjacent bands are subtracted, very small changes in the pixel values become important. These small changes may be strongly influenced by image noise.

9. The confusion matrices show that the predicted age classes for younger stands tended to be biassed upwards, and the predicted age classes for older stands tended to be biassed downwards.

CHAPTER IV: Conclusions

The research conducted for this thesis attempted to determine whether artificial neural networks could be used to predict the ages of forest stands in a hyperspectral image. Results show that stand ages can be accurately predicted, although the accuracy of the predictions may not be suitable for some applications. This technique may be useful for practical forestry in situations when ground data are available, but acquiring and interpreting air photos are prohibitively expensive. The utility of this method will increase once satellite-mounted hyperspectral sensor such as Hyperion, OrbView 4 and the Naval Earth Map Observer (NEMO) are launched in late 2000 and 2001.

There are several potential avenues for future research. From an operational standpoint, it would be exceedingly useful to redo the analysis using stand ages obtained on the ground rather than from air photos. This would eliminate photo interpretation errors and would more closely duplicate the foreseen use of this procedure. Additionally, experiments could be performed to determine whether the accuracy increases if more training data were used, and if so to quantify this increase.

One problem the approach taken by this paper is that overfitting was not well addressed. Future attempts could attempt to better address this by using either the early stopping technique, adding white noise to the input data (Sarle, 2000). Repeating the experiment using conventional statistics may also be instructive.

BIBLIOGRAPHY

Atkinson, P. M. and A. R. L. Tatnall. 1997. Neural networks in remote sensing. Int. J. Remote Sensing 18: 699-709.

Avery, T. E. and G. L. Berlin. 1992. Fundamentals of Remote Sensing and Airphoto interpretation, Fifth Edition. New York: Macmillan. 472p.

Barton, F. E. (II). D. S. Himmelsbach. J. H. Duckworth. M. J. Smith. Two-dimensional vibration spectroscopy: Correlation of mid- and near-infrared regions. Applied Spectroscopy 46: 420-429.

BC Ministry of Forests. 1995a. Bark Beetle Management Guidebook. http://www.for.gov.bc.ca/tasb/legsregs/fpc/fpcguide/beetle/beetletoc.htm.

BC Ministry of Forests. 1995b. Biodiversity Guidebook. http://www.for.gov.bc.ca/tasb/legsregs/fpc/fpcguide/biodiv/diotoc.htm.

BC Ministry of Forests. 1995c. Defoliator Management Guidebook. http://www.for.gov.bc.ca/tasb/legsregs/fpc/fpcguide/defoliat/defoltoc.htm.

BC Ministry of Forests. 1996. Pine Stem Rust Management Guidebook. http://www.for.gov.bc.ca/tasb/legsregs/fpc/fpcguide/pinestem/pine-toc.htm.

BC Ministry of Forests. 1998a. Chapter 2: Preparation of forest cover source maps." In The Preparation and Creation of FRGIS Data Files. Victoria: Crown Publications.

BC Ministry of Forests. 1998b. Vegetation Resources Inventory Photo Interpretation Standards (v1.0). http://www.for.gov.bc.ca/ric/pubs/teveg/PhotoStandards/index.htm

BC Ministry of Forests. 1999. Vegetation Resources Inventory Photo Interpretation Procedures (v2.2). http://www.for.gov.bc.ca/RIC/Pubs/teveg/VRI_PhotoInterp/index.htm.

Billingsley, F. C.. 1983. "Data processing and reprocessing." In Colwell, R. N.. (Editor) Manual of Remote Sensing. Second Edition, Vol. 1. Falls Church, VA: American Society of Photogrammetry. pp. 719-792.

Bosch, E. H.. 1995. The effects different neural network architectures have on the exploitation of hyperspectral data. International Symposium on Spectral Sensing Research '95 Reports.

Brockhaus, J. A. and S. Khorram. 1992 A comparison of SPOT and Landsat TM data for use in conducting inventories of forest resources." Int. J. Remote Sensing 13: 3035-3043.

Clark, R. N.. K. E. Livo. R. F. Kokaly. 1998. Geometric correction of AVIRIS imagery using on-board navigation and engineering data. Summaries of the 7th Annual Airborne Earth Science Workshop.

Clark, R. N.. 1999. Spectroscopy of Rocks and Minerals, and Principles of Spectroscopy. http://speclab.cr.usgs.gov/PAPERS.refl-mrs/refl4.html.

Cohen, W. B.. T. A. Spies. 1992. Estimating structural attributes of Douglas-fir / western hemlock forest stands from Landsat and SPOT imagery. Remote Sens. Environ. 41: 1-17.

Cohen, W. B.. T. A. Spies. M. Fiorella. 1995. Estimating the age and structure of forests in a multi-ownership landscape of western Oregon, U.S.A." Int. J. Remote Sensing 16: 721-746.

Collins, W.. 1978. Remote sensing of crop type and maturity. Photogrammetric Engin. and Remote Sens. 44: 43-55.

Danson, F. M.. 1987. Preliminary evaluation of the relationships between SPOT-1 HRV data and forest stand parameters. Int. J. Remote Sensing 8: 1571-1575.

Davis, J. C.. 1986. Statistics and Data Analysis in Geology. New York: Wiley. 656p.

DeWulf, R. R.. R. E. Goossens. B. P. DeRoover. F. C. Borry. 1990. Extraction of forest stand parameters from panchromatic and multispectral SPOT-1 data." Int. J. Remote Sensing 11: 1571-1588.

Fiorella, M.. W. J. Ripple. 1993. Determining successional stage of temperate coniferous forests with Landsat satellite data. Photogrammetric Engin. and Remote Sens. 59: 239-246.

Gao, B.-C.. K. B. Heidebrecht. A. F. H. Goetz. 1997. Atmosphere Removal Program (ATREM) Version 3.0 User's Guide. Boulder: University of Colorado. 26p.

Gates, D. M.. H. J. Keegan. J. C. Schleter. V. R. Weidner. 1965. Spectral properties of plants. Applied Optics 4: 11-19.

Gong, P., R. Pu, B. Yu. 1997. Conifer species recognition: Exploratory analysis of *in situ* hyperspectral data. Remote Sens. Environ. 62: 189-200.

Grant, L.. 1987. Diffuse and specular characteristics of leaf reflectance. Remote Sens. Environ. 22: 309-322.

Green, R. O. and D. A. Roberts. 1995. Vegetation species composition and canopy architecture information expressed in leaf water absorption measured in the 1000 nm and 2200 nm spectral region by an imaging spectrometer." 1995 Airborne Geoscience Workshop Proceedings.

Green, R. O. M. L. Eastwood. C. M. Sarture, T. G. Chrien. M. Aronsson. B. J. Chippendale. J. A. Faust. B. E. Pavri. C. J. Chovit. M. S. Solis. M. R. Olah. O. Williams. 1998. Imaging spectroscopy and the Airborne Visible/Infrared Imaging Spectrometer (AVIRIS). Remote Sens. Environ. 65: 227-248.

Guyot, G. and D. G. J. Riom. 1989. Factors affecting the spectral response of forest canopies: A review. Geocarto International 4: 3-18.

Hallett, R. A.. J. W. Hornbeck. M. E. Martin. 1997. Predicting elements in white pine and red oak foliage with visible-near infrared reflectance spectroscopy. J. Near Infrared Spectrosc. 5: 77-82.

Halopainen, M.. 1998. Forest habitat classification by CASI airborne measurements. For. and Landsc. Res. 1: 431-446.

Horler, D. N. H.. M. Dockray. J. Barber. 1983. The red edge of plant leaf reflectance. Int. J. Remote Sensing 4: 273-288.

Jensen, C.. 1999. QwikNet v2.23 User's Manual.

Johnson, L. F., C. A. Hlavka and D. L. Peterson. 1994. Multivariate analysis of AVIRIS data for canopy biochemical estimation along the Oregon Transect. Remote Sens. Environ. 47: 216-230.

Kanellopoulos, I and G. G. Wilkinson. 1997. Strategies and best practice for neural network image classification. Int. J. Remote Sensing 18: 711-725.

Kimes, D. S.. B. N. Holbin. J. E. Nickeson. W. A. McKee. 1996. Extracting forest age in a Pacific Northwest forest from Thematic Mapper and topographic data. Remote Sens. Environ. 56: 133-140.

Kimes, D. S. and Nelson, R. F. 1998. Attributes of neural networks for extracting continuous vegetation, Int. J. Remote Sensing, 19: 2639-2663.

Lawlor, D. W.. 1987. Photosynthesis: Metabolism, Control and Physiology. Essex,

England: Longman. 262pp.

Long, J. N. and J. Turner. 1975. Above-ground biomass of understory and overstory in an age sequence of Douglas-fir stands. J. Applied Ecology 12:179-188.

Masters, T.. 1993. Practical Neural Network Recepies in C++. San Diego: Academic Press. 493p.

Murtha, P. A.. D. W. Deering. C. E. Olson Jr.. G. A. Bracher. 1997. Vegetation. In Philipson, W. R.. (ed.) Manual of Photographic Interpretation (Second Edition.) Bethesda, Maryland: American Society for Photogrammetry and Remote Sensing. pp. 225-255.

National Aeronautics and Space Administration. 2000. The Remote Sensing Tutorial. http://rst.gsfc.nasa.gov/

Niemann, K. O.. 1995. Remote sensing of forest stand age using airborne spectrometer data. Photogrammetric Engin. and Remote Sens. 61: 1119-1127.

Ott, R. L.. 1993. An Introduction to Statistical Methods and Data Analysis. Belmont, California: Duxbury Press. 1051p.

Richards, J. A. and X. Jia.. 1999. Remote Sensing Digital Image Analysis: An Introduction. Berlin: Springer-Verlag. 363p.

Rumelhart, D. E.. G. E. Hinton. R. L. Williams. 1986. Learning internal representations by error propagation. In Rumelhart, D. E. and J. L. McClelland (eds.) Parallel Distributed Processing: Explorations in the Microstructures of Cognition (Vol. 1) Cambridge, MA: MIT Press. pp. 318-362.

Running, S. W.. D. L. Paterson. M. A. Spanner. K. B. Teuber. 1986. Remote sensing of coniferous forest leaf area. Ecology 67: 273-276.

Sarle, W. S.. 2000. Neural Networks FAQ. ftp://ftp.sas.com/pub/neural/FAQ.html.

Wessman, C. A.. J. D. Aber. D. L. Peterson. J. M. Melillo. 1988. Foliar analysis using near infrared reflectance spectroscopy. Can. J. For. Res. 18: 6-11.

Yang, H.. F. Van Der Meer. W. Bakker. Z. J. Tan. 1999. A back-propagation ne ural network for mineralogical mapping from AVIRIS data. Int. J. Remote Sensing 20: 97-110.

Zagolski, F., V. Pinel, J. Romier, D. Alcayde, J. Fontanari, J. P. Gastellu-Etchegorry, G.

Giordano, G. Marty, E. Mougin and R. Joffre. 1996. Forest canopy chemistry with high spectral resolution remote sensing. Int. J. Remote Sensing 17: 1107-1128.

APPENDIX I: Wavelengths of the AVIRIS channels used in the study

The bands indicated as noisy were excluded (see text).

Band	Wavelength (mm)	Change in wavelength (mm)	Noisy?
1	0.383940	0.009310	Yes
2	0.393430	0.009310	Yes
3	0.402970	0.009310	Yes
4	0.412530	0.009310	Yes
5	0.422130	0.009310	Yes
6	0.431760	0.009310	Yes
7	0.441420	0.009310	Yes
8	0.451100	0.009310	Yes
9	0.460810	0.009310	Yes
10	0.470550	0.009310	Yes
11	0.480300	0.009310	Yes
12	0.490080	0.009310	Yes
13	0.499870	0.009310	Yes
14	0.509680	0.009310	Yes
15	0.519510	0.009310	Yes
16	0.529350	0.009310	No
17	0.539200	0.009310	No
18	0.549060	0.009310	No
19	0.558930	0.009310	No
20	0.568810	0.009300	No
21	0.578690	0.009300	No
22	0.588570	0.009300	No
23	0.598460	0.009300	No
24	0.608340	0.009300	No
25	0.618230	0.009300	No
26	0.628110	0.009300	No
27	0.637980	0.009300	No
28	0.647850	0.009300	No
29	0.657710	0.009300	No
30	0.667560	0.009300	No
31	0.677400	0.009300	No
32	0.687220	0.009300	No
33	0.664790	0.008820	Yes
34	0.674380	0.008820	No
35	0.683980	0.008830	No
36	0.693580	0.008830	No
37	0.703170	0.008830	No
38	0.712770	0.008840	No
39	0.722370	0.008840	No

40	0.731960	0.008840	No
41	0.741560	0.008850	No
42	0.751160	0.008850	No
43	0.760752	0.008860	No
44	0.770350	0.008860	No
45	0.779950	0.008860	No
46	0.789550	0.008870	No
47	0.799140	0.008870	No
48	0.808740	0.008870	No
49	0.818340	0.008880	No
50	0.827940	0.008880	No
51	0.837540	0.008880	No
52	0.847130	0.008890	No
53	0.856730	0.008890	No
54	0.866330	0.008890	No
55	0.875930	0.008900	No
56	0.885530	0.008900	No
57	0.895130	0.008900	No
58	0.904730	0.008910	No
59	0.914330	0.008910	No
60	0.923930	0.008910	No
61	0.933530	0.008920	No
62	0.943130	0.008920	No
63	0.952730	0.008930	No
64	0.962330	0.008930	No
65	0.971930	0.008930	No
66	0.981530	0.008940	No
67	0.991130	0.008940	No
68	1.000730	0.008940	No
69	1.010330	0.008950	No
70	1.019930	0.008950	No
71	1.029530	0.008950	No
72	1.039140	0.008960	No
73	1.048740	0.008960	No
74	1.058340	0.008960	No
75	1.067940	0.008970	No
76	1.077540	0.008970	No
77	1.087150	0.008970	No
78	1.096754	0.008980	No
79	1.106350	0.008980	No
80	1.115950	0.008980	No
81	1.125560	0.008990	No
82	1.135160	0.008990	No
83	1.144760	0.009008	No

84	1.154370	0.009008	No
85	1.163970	0.009008	No
86	1.173570	0.009010	No
87	1.183180	0.009010	No
88	1.192780	0.009010	No
89	1.202390	0.009020	No
90	1.211990	0.009020	No
91	1.221590	0.009020	No
92	1.231200	0.009030	No
93	1.240800	0.009030	No
94	1.250410	0.009030	No
95	1.260010	0.009040	No
96	1.269620	0.009040	No
97	1.253300	0.009650	Yes
98	1.263260	0.009660	No
99	1.273230	0.009670	No
100	1.283190	0.009680	No
101	1.293140	0.009690	No
102	1.303100	0.009700	No
103	1.313050	0.009710	No
104	1.323010	0.009720	No
105	1.332960	0.009730	No
106	1.342910	0.009730	No
107	1.352850	0.009740	Yes
108	1.362800	0.009758	Yes
109	1.372740	0.009760	Yes
110	1.382690	0.009770	Yes
111	1.392630	0.009780	Yes
112	1.402570	0.009790	Yes
113	1.412510	0.009800	Yes
114	1.422440	0.009810	Yes
115	1.432380	0.009820	Yes
116	1.442320	0.009830	Yes
117	1.452254	0.009840	No
118	1.462190	0.009850	No
119	1.472120	0.009850	No
120	1.482050	0.009860	No
121	1.491980	0.009870	No
122	1.501910	0.009880	No
123	1.511850	0.009890	No
124	1.521780	0.009900	No
125	1.531710	0.009910	No
126	1.541640	0.009920	No
127	1.551570	0.009930	No

128	1.561504	0.009940	No
129	1.571430	0.009950	No
130	1.581360	0.009960	No
131	1.591290	0.009970	No
132	1.601220	0.009970	No
133	1.611150	0.009980	No
134	1.621080	0.009990	No
135	1.631010	0.010008	No
136	1.640950	0.010010	No
137	1.650880	0.010020	No
138	1.660810	0.010030	No
139	1.670754	0.010040	No
140	1.680680	0.010050	No
141	1.690620	0.010060	No
142	1.700560	0.010070	No
143	1.710490	0.010080	No
144	1.720430	0.010090	No
145	1.730370	0.010100	No
146	1.740320	0.010100	No
147	1.750260	0.010110	No
148	1.760200	0.010120	No
149	1.770150	0.010130	No
150	1.780100	0.010140	No
151	1.790050	0.010150	No
152	1.801004	0.010160	No
153	1.809950	0.010170	Yes
154	1.819910	0.010180	Yes
155	1.829870	0.010190	Yes
156	1.839830	0.010200	Yes
157	1.849790	0.010210	Yes
158	1.859754	0.010220	Yes
159	1.869720	0.010220	Yes
160	1.879680	0.010230	Yes
161	1.876630	0.011980	Yes
162	1.886550	0.011980	Yes
163	1.896480	0.011980	Yes
164	1.906400	0.011980	Yes
165	1.916320	0.011980	Yes
166	1.926240	0.011980	Yes
167	1.936160	0.011980	Yes
168	1.946080	0.011980	Yes
169	1.956004	0.011980	Yes
170	1.965920	0.011980	Yes
171	1.975840	0.011970	No

172	1.985760	0.011970	No
173	1.995680	0.011970	No
174	2.005600	0.011970	Yes
175	2.015520	0.011970	No
176	2.025440	0.011970	No
177	2.035360	0.011970	No
178	2.045280	0.011970	No
179	2.055200	0.011970	No
180	2.065120	0.011970	No
181	2.075040	0.011970	No
182	2.084960	0.011970	No
183	2.094880	0.011970	No
184	2.104800	0.011960	No
185	2.114720	0.011960	No
186	2.124640	0.011960	No
187	2.134560	0.011960	No
188	2.144490	0.011960	No
189	2.154410	0.011960	No
190	2.164330	0.011960	No
191	2.174258	0.011960	No
192	2.184170	0.011960	No
193	2.194090	0.011960	No
194	2.204010	0.011960	No
195	2.213930	0.011960	No
196	2.223850	0.011960	No
197	2.233770	0.011950	No
198	2.243690	0.011950	No
199	2.253610	0.011950	No
200	2.263530	0.011950	No
201	2.273450	0.011950	No
202	2.283370	0.011950	No
203	2.293290	0.011950	No
204	2.303210	0.011950	No
205	2.313130	0.011950	No
206	2.323050	0.011950	No
207	2.332970	0.011950	No
208	2.342890	0.011950	No
209	2.352810	0.011950	No
210	2.362730	0.011940	No
211	2.372650	0.011940	No
212	2.382570	0.011940	No
213	2.392508	0.011940	No
214	2.402420	0.011940	No
215	2.412340	0.011940	Yes

216	2.422260	0.011940	Yes
217	2.432180	0.011940	Yes
218	2.442100	0.011940	Yes
219	2.452020	0.011940	Yes
220	2.461940	0.011940	Yes
221	2.471860	0.011940	Yes
222	2.481780	0.011940	Yes
223	2.491700	0.011930	Yes
224	2.501620	0.011930	Yes

APPENDIX II: Results for polygons containing pure Douglas-fir stands

The architecture column refers to the number of hidden nodes. The hidden nodes are arranged in a single layer except where two numbers are given, in which case the numbers give the number of hidden nodes in the first and second hidden layer respectively. Please see text for an explanation of the other columns. Correlation coefficients which are not significant at the $\alpha = 0.05$ level have been italicised.

Data	Architecture	Learning rate	RMS: All polygons		RMS: Area > 10000 m²		RMS: Area > 40000 m²	
			Frequency	*Mean*	*Frequency*	*Mean*	Frequency	Mean
Reflectance, topo, angle	3	0.1	2.53	2.01	2.31	1.90	1.77	1.61
	4	0.1	2.72	1.84	2.47	1.72	1.68	1.38
	5	0.1	2.63	2.12	2.78	2.03	1.92	1.82
	10	0.1	2.99	2.03	2.57	1.90	2.03	1.64
	20	0.1	2.79	1.92	2.57	1.81	1.76	1.54
	10 and 5	0.1	3.19	2.03	3.00	1.87	2.31	1.54
	50	0.3	2.92	2.13	2.64	1.94	1.93	1.64
Reflectance, topo, angle	3	0.2	3.07	2.10	2.87	1.97	2.50	1.73
	4	0.2	2.98	2.00	2.78	1.86	2.16	1.61
	5	0.2	2.99	2.05	2.71	1.82	1.96	1.51
	10	0.2	3.01	2.06	2.77	1.79	2.07	1.47
	20	0.2	3.05	2.04	2.76	1.86	1.81	1.50
	10 and 5	0.2	3.18	1.97	3.02	1.82	2.27	1.51
Reflectance only	3	0.1	2.80	1.98	2.63	1.87	2.04	1.60
	4	0.1	3.07	1.99	2.87	1.85	2.28	1.64
	5	0.1	3.10	2.00	2.86	1.83	2.00	1.50
	10	0.1	3.05	2.00	2.84	1.85	1.98	1.51
	20	0.1	2.94	1.95	2.77	1.82	2.04	1.53
	10 and 5	0.1	3.02	1.92	2.78	1.75	1.93	1.47
First difference	3	0.1	2.53	2.13	3.11	1.97	2.38	1.75
	4	0.1	2.72	2.09	3.26	1.96	2.70	1.74
	5	0.1	2.63	2.28	3.32	2.12	2.89	1.94

	10	0.1	2.99	2.20	3.27	2.04	2.63	1.81
	20	0.1	2.79	2.28	3.41	2.14	2.87	1.95
	10 and 5	0.1	3.36	2.15	3.12	1.97	2.56	1.79
Simulated Landsat TM	3	0.1	3.71	3.21	3.47	3.12	3.59	3.16
plus topo and angle	4	0.1	3.33	3.14	3.30	3.05	3.39	3.11
	5	0.1	3.57	3.18	3.84	3.35	3.93	3.36
	10	0.1	3.85	3.19	4.20	3.33	4.32	3.44
	20	0.1	4.34	3.39	4.42	3.34	4.30	3.35
	10 and 5	0.1	4.32	3.26	4.38	3.36	4.41	3.53
Visible and IR plus	3	0.1	2.49	2.13	2.37	1.98	1.79	1.68
topo and angle	4	0.1	2.64	2.18	2.36	2.01	1.75	1.67
	5	0.1	2.87	2.24	2.58	2.07	2.04	1.77
	10	0.1	2.76	2.03	2.41	1.79	1.86	1.54
	20	0.1	3.02	2.13	2.75	1.87	1.73	1.54
	10 and 5	0.1	2.97	2.04	2.68	1.75	1.96	1.48

Data	**Architecture**	**Learning rate**	**r_s: All polygons**		**r_s: Area > 10000 m^2**		**r_s: Area > 40000 m^2**	
			Frequency	*Mean*	*Frequency*	*Mean*	*Frequency*	*Mean*
Reflectance, topo, angle	3	0.1	0.5615	0.6596	0.6376	0.7067	0.7448	0.7956
	4	0.1	0.5347	0.6708	0.5993	0.7074	0.7299	0.8029
	5	0.1	0.5352	0.6368	0.5949	0.6869	0.7030	0.7861
	10	0.1	0.4583	0.6322	0.5317	0.6763	0.6929	0.7751
	20	0.1	0.5160	0.6319	0.5787	0.6857	0.7088	0.7842
	10 and 5	0.1	0.4969	0.6226	0.5316	0.6835	0.6637	0.7811
	50	0.3	0.5797	0.6163	0.6979	0.6299	0.7333	0.8023
Reflectance, topo, angle	3	0.2	0.5104	0.6090	0.5496	0.6668	0.6208	0.7519
	4	0.2	0.5247	0.6181	0.5522	0.6719	0.6878	0.7639
	5	0.2	0.5253	0.6248	0.5971	0.7124	0.7241	0.7936
	10	0.2	0.5251	0.6112	0.5702	0.6917	0.6825	0.7833
	20	0.2	0.5604	0.6145	0.6092	0.6869	0.7473	0.7849
	10 and 5	0.2	0.4875	0.6381	0.5188	0.6978	0.6727	0.7860

Reflectance only	3	0.1	0.5699	0.6525	0.6089	0.6893	0.7081	0.7777
	4	0.1	0.5490	0.6490	0.5824	0.7023	0.6884	0.7807
	5	0.1	0.5664	0.6393	0.6102	0.6949	0.7433	0.7829
	10	0.1	0.5232	0.6433	0.5651	0.6942	0.7108	0.7907
	20	0.1	0.5620	0.6451	0.59	0.6975	0.713	0.79
	10 and 5	0.1	0.5245	0.6546	0.5769	0.7156	0.7225	0.7985
First difference	3	0.1	0.5615	0.6357	0.5755	0.6900	0.7077	0.7839
	4	0.1	0.5347	0.6163	0.5489	0.6626	0.6428	0.7548
	5	0.1	0.5352	0.6363	0.5915	0.6948	0.6612	0.7964
	10	0.1	0.4583	0.6383	0.5989	0.7045	0.6944	0.7971
	20	0.1	0.516	0.6268	0.5444	0.6838	0.6509	0.7826
	10 and 5	0.1	0.5021	0.6436	0.5463	0.7218	0.6422	0.7960
Simulated Landsat TM	3	0.1	0.1180	0.1509	0.0949	0.0973	0.127	0.1309
plus topo and angle	4	0.1	0.1431	0.1215	0.1148	*0.0770*	0.1209	*0.0660*
	5	0.1	0.1526	0.1038	0.0936	0.0862	*0.1036*	0.1271
	10	0.1	0.0847	*0.0555*	*0.0550*	*0.0199*	*0.0201*	*0.0084*
	20	0.1	*0.0088*	*0.0229*	*0.0397*	*0.0827*	*0.0846*	*0.1107*
	10 and 5	0.1	0.0904	0.1042	*0.0540*	*0.0670*	*0.0572*	*0.0340*
Visible / NIR plus	3	0.1	0.4864	0.5894	0.6072	0.6295	0.7211	0.7372
topo and angle	4	0.1	0.4856	0.5945	0.6029	0.6518	0.7307	0.7621
	5	0.1	0.4856	0.5932	0.6030	0.6575	0.7111	0.7596
	10	0.1	0.5074	0.646	0.6025	0.6754	0.7099	0.7724
	20	0.1	0.4819	0.6229	0.5788	0.6674	0.7677	0.7949
	10 and 5	0.1	0.4450	0.6262	0.5571	0.6814	0.7031	0.7859

APPENDIX III: Results for all polygons regardless of species present

The architecture column refers to the number of hidden nodes. The hidden nodes are arranged in a single layer except where two numbers are given, in which case the numbers give the number of hidden nodes in the first and second hidden layer respectively. Please see text for an explanation of the other columns. Correlation coefficients which are not significant at the $\alpha = 0.05$ level have been italicised.

Data	Architecture	Learning rate	RMS: All polygons		RMS: Area > 10000 m^2		RMS: Area > 40000 m^2	
			Frequency	*Mean*	*Frequency*	*Mean*	*Frequency*	*Mean*
Reflectance plus topo and angle	3	0.1	3.31	2.21	3.18	2.08	2.50	1.86
	4	0.1	2.52	2.33	3.43	2.19	2.8	1.97
	5	0.1	3.66	2.28	3.53	2.10	2.82	1.74
	10	0.1	3.56	2.07	3.47	1.89	2.72	1.58
	20	0.1	3.57	2.27	3.44	2.09	2.59	1.80
	10 and 5	0.1	3.66	2.10	3.56	1.94	2.91	1.74
Reflectance only	3	0.1	4.22	2.14	2.90	1.99	2.18	1.77
	4	0.1	4.29	1.94	2.71	1.77	1.92	1.55
	5	0.1	4.45	2.04	3.14	1.89	2.31	1.67
	10	0.1	4.52	2.03	3.33	1.87	2.44	1.62
	20	0.1	4.54	1.98	3.43	1.81	2.54	1.53
	10 and 5	0.1	4.45	1.97	3.38	1.83	2.51	1.57
First difference	3	0.1	4.05	2.21	3.96	2.18	3.22	2.03
	4	0.1	4.01	2.20	3.94	2.11	3.29	1.93
	5	0.1	4.05	2.29	3.95	2.17	3.19	2.03
	10	0.1	3.56	2.27	3.47	2.19	2.72	1.99
	20	0.1	3.57	2.29	3.44	2.20	2.59	2.05
	10 and 5	0.1	4.05	2.34	3.97	2.24	3.36	2.10
Simulated Landsat TM plus topo and angle	3	0.1	2.26	2.22	2.14	2.14	1.91	1.95
	4	0.1	2.31	2.25	2.18	2.16	1.89	1.97
	5	0.1	2.47	2.29	2.33	2.22	2.01	2.00
	10	0.1	2.50	2.19	2.36	2.17	1.95	1.79
	20	0.1	2.61	2.14	2.44	2.05	1.76	1.75

	10 and 5	0.1	3.03	2.25		2.44	2.03		2.32	1.85
Visible / NIR plus	3	0.1	2.91	2.59		2.78	2.51		2.27	2.22
topo and angle	4	0.1	2.18	2.19		2.08	2.11		1.67	1.86
	5	0.1	2.56	2.45		2.42	2.34		1.83	1.99
	10	0.1	3.17	2.40		3.05	2.32		2.35	2.00
	20	0.1	3.28	2.36		3.13	2.23		2.38	1.86
	10 and 5	0.1	3.21	2.19		3.11	2.08		2.55	1.88

Data	Architecture	Learning rate	r_s: All polygons		r_s: Area > 10000 m^2		r_s: Area > 40000 m^2	
			Frequency	Mean	Frequency	Mean	Frequency	Mean
Reflectance plus	3	0.1	0.4314	0.6332	0.4746	0.6806	0.6526	0.7756
topo and angle	4	0.1	0.4005	0.5350	0.4358	0.5913	0.6180	0.7077
	5	0.1	0.4280	0.6260	0.4534	0.6732	0.6033	0.7745
	10	0.1	0.4201	0.6582	0.4451	0.7039	0.6097	0.8036
	20	0.1	0.3381	0.5381	0.3630	0.5950	0.5651	0.7262
	10 and 5	0.1	0.3293	0.6612	0.3605	0.7137	0.5658	0.8000
Reflectance only	3	0.1	*0.0013*	0.6686	0.5646	0.7193	0.7316	0.8014
	4	0.1	*0.0231*	0.6883	0.5566	0.7365	0.7280	0.8194
	5	0.1	*0.0084*	0.6800	0.5234	0.7299	0.6905	0.8179
	10	0.1	*0.0216*	0.6631	0.4832	0.7091	0.6668	0.8045
	20	0.1	*0.0457*	0.6715	0.4520	0.7186	0.6346	0.8157
	10 and 5	0.1	0.0592	0.6946	0.4486	0.7421	0.6603	0.8374
First difference	3	0.1	0.3503	0.6142	0.3618	0.6624	0.5425	0.7644
	4	0.1	0.3891	0.6267	0.4051	0.6583	0.5403	0.7593
	5	0.1	0.3653	0.5945	0.3949	0.6588	0.5720	0.7797
	10	0.1	0.4201	0.6218	0.4451	0.6567	0.6097	0.7776
	20	0.1	0.3381	0.6190	0.3630	0.6662	0.5651	0.7782
	10 and 5	0.1	0.3695	0.6176	0.3861	0.6727	0.5228	0.7784
Simulated Landsat TM	3	0.1	0.5543	0.5945	0.5863	0.6336	0.6991	0.7526
plus topo and angle	4	0.1	0.5604	0.5944	0.5958	0.6347	0.7095	0.7518
	5	0.1	0.5440	0.5931	0.5827	0.6273	0.6228	0.7403
	10	0.1	0.5312	0.5976	0.5624	0.628	0.6974	0.7508
	20	0.1	0.5129	0.6074	0.5749	0.6488	0.7361	0.7752
	10 and 5	0.1	0.4426	0.6035	0.4777	0.6374	0.6485	0.7630

Visible / NIR plus	3	0.1	0.4864	0.5887	0.5583	0.6081	0.6854	0.7183
topo and angle	4	0.1	0.6412	0.6430	0.6615	0.6675	0.7754	0.7738
	5	0.1	0.6028	0.6122	0.6261	0.6457	0.7524	0.7567
	10	0.1	0.5207	0.6207	0.5383	0.6336	0.6930	0.7409
	20	0.1	0.4850	0.6113	0.5154	0.6412	0.6651	0.7557
	10 and 5	0.1	0.4694	0.6383	0.4958	0.6730	0.6404	0.7682

APPENDIX IV: GLOSSARY OF TERMS

Aerosol: Fine particles of a solid or liquid which are suspended in a gas.

Albedo: The fraction of incident energy which is reflected.

Azimuth angle: The angle between due south and the direction of the sun.

Byte order: In digital numbers containing two or more bytes, one byte (or group of bytes) contains information on the smaller portion of a number, and the other byte (or group of bytes) contains information on the larger portion of the number. The order in which these bytes are stored is called the byte order. There are two byte orders in use: little-endian byte order stores the smaller portion of number first and big-endian stores the larger portion of the number first

Classification: The process of converting the spectral and / or spatial information in a remotely sensed image into surface cover data. Computerized classification can be divided into two categories: unsupervised classification in which information about the surface cover is not used and supervised classification in which surface information is used to create the classes.

Combination: A spectral absorption feature which is at a frequency equal to the sum of two primary absorption features.

Confusion matrix: A table which shows the number of units (e.g. pixels) assigned to a category in relation to their true categories.

Delocalised electrons: Delocalised electrons are electrons which orbit a molecule or a portion of a molecule rather than the nucleus of an atom.

Digital number (DN) value: The value associated with a single pixel of a multispectral image or with a pixel in a single band of a multispectral image. In most circumstances the DN value is directly related to the amount of at sensor radiance received by the sensor at the pixel's location.

False colour: An image in which the brightness of the red layer corresponds to the reflectance or at sensor radiance in the near-infrared spectral region, the green layer corresponds to the reflectance or at sensor radiance in the red spectral region, and the blue layer corresponds to the reflectance or at sensor radiance in the green spectral region.

Flux: The rate of flow of an entity through a given surface area.

GPS: An acronym for Global Positioning System. An instrument which uses satellite radio signals to determine its geographic location.

Grana: These are structures found in the leaf's chloroplasts which consist of an alternating layer of lipid, chlorophyll and protein.

Lambertian: A surface which reflects incident light equally in all directions.

Landsat Thematic Mapper (TM): A multispectral sensor included on the Landsat III through V satellites. It has a spatial resolution of 30m and includes seven bands:

Band 1	0.45 - 0.52 μm
Band 2	0.52 - 0.60 μm
Band 3	0.63 - 0.69 μm
Band 4	0.76 - 0.90 μm
Band 5	1.55 - 1.75 μm
Band 6	10.40 - 12.50 μm
Band 7	2.08 - 2.35 μm

Mesophyll: The area of a leaf between the upper and lower epidermis.

Multispectral: A sensor containing bands sensitive to different portions of the electromagnetic spectrum.

Overtone: A spectral absorption feature at a frequency which is a multiple of the frequency of the primary vibrational absorption.

Panchromatic: A sensor containing a single band sensitive to a single wavelength region.

Pitch: The angle between the body of an aircraft in flight and a plane parallel to the earth's surface.

Primary species: The commercial or brush species with the highest volume per hectare or number of stems (for young stands) in a polygon.

Radiance: The flux of electromagnetic energy which exits a body in a given direction.

Radiative transfer model: A model which addresses the interaction of electromagnetic radiation with an atmosphere.

Raster: An image consisting of a grid of pixels.

Refraction: The bending of light when light passes from one material into a material in which the velocity of light differs. The index of refraction is the ratio the speed of light in a vacuum to the speed of light in a material of interest.

Roll: The angle between the wings of an aircraft in flight and plane parallel to the earth's surface.

Secondary species: The commercial or brush species with the second highest volume per hectare or number of stems (for young stands) in a polygon.

Spatial autocorrelation: The degree to which objects which are closer together resemble eachother more than objects which are further apart.

Spectrometer: An instrument used for measuring the radiance of light at different wavelengths.

SPOT 1: An acronym for La Système Pour L'Observation de la Terre 1. It is a French satellite containing one high resolution panchromatic band and three multispectral bands. The spatial resolution is 10 m for the panchromatic band and 20 m for the multispectral band. The wavelengths for the multispectral bands are:

Band 1	0.50 - 0.59 μm
Band 2	0.61 - 0.68 μm
Band 3	0.79 - 0.89 μm

Tassled cap: A series of linear transformations of the original DN values in a multispectral image. These transformations create a series of images highlighting spectral information useful for vegetation remote sensing. In the Landsat Tm tasseled cap, the amount of green vegetation (greenness), exposed soil (brightness), leaf water (wetness) and the noise / haze (none-such) are emphasised.

Texture: A measurement which is related to the difference in the DN values associated with pixels in a neighbourhood.

Wavelength: In a wave, this is the distance between subsequent troughs or peaks.

Zenith angle: The angle between the centre of the sun and a point directly above a location on the earth's surface.